



**UNIVERSIDAD DE INVESTIGACIÓN DE TECNOLOGÍA
EXPERIMENTAL YACHAY**

Escuela de Ciencias de la Tierra, Energía y Ambiente

**TÍTULO: The First Electrical Resistivity Tomography Study
Applied to an Ecuadorian Cave (Uctu Iji Changa, Tena): Insights
into Amazonian Karst Systems**

Trabajo de integración curricular presentado como requisito para
la obtención del título de Geólogo

Autor:

Chamba Vásquez Bryan Antonio

Tutor:

Elisa Johanna Piispa, Ph.D

Urququí, Septiembre 2020

Urcuquí, 2 de septiembre de 2020

SECRETARÍA GENERAL
(Vicerrectorado Académico/Cancillería)
ESCUELA DE CIENCIAS DE LA TIERRA, ENERGÍA Y AMBIENTE
CARRERA DE GEOLOGÍA
ACTA DE DEFENSA No. UITEY-GEO-2020-00012-AD

A los 2 días del mes de septiembre de 2020, a las 10:00 horas, de manera virtual mediante videoconferencia, y ante el Tribunal Calificador, integrado por los docentes:

Presidente Tribunal de Defensa	Dr. TORO ALAVA, JORGE EDUARDO , Ph.D.
Miembro No Tutor	Dr. PINEDA ORDOÑEZ, LUIS EDUARDO , Ph.D.
Tutor	Dra. PIISPA , ELISA JOHANNA , Ph.D.

El(la) señor(ita) estudiante **CHAMBA VASQUEZ, BRYAN ANTONIO**, con cédula de identidad No. 1717876856, de la **ESCUELA DE CIENCIAS DE LA TIERRA, ENERGÍA Y AMBIENTE**, de la Carrera de **GEOLOGÍA**, aprobada por el Consejo de Educación Superior (CES), mediante Resolución RPC-SE-10-No.031-2016, realiza a través de videoconferencia, la sustentación de su trabajo de titulación denominado: **ELECTRICAL RESISTIVITY TOMOGRAPHY SURVEY APPLIED TO A CAVE (UCTU IJI CHANGA) IN TENA, ECUADOR**, previa a la obtención del título de **GEÓLOGO/A**.

El citado trabajo de titulación, fue debidamente aprobado por el(los) docente(s):

Tutor	Dra. PIISPA , ELISA JOHANNA , Ph.D.
-------	-------------------------------------

Y recibió las observaciones de los otros miembros del Tribunal Calificador, las mismas que han sido incorporadas por el(la) estudiante.

Previamente cumplidos los requisitos legales y reglamentarios, el trabajo de titulación fue sustentado por el(la) estudiante y examinado por los miembros del Tribunal Calificador. Escuchada la sustentación del trabajo de titulación a través de videoconferencia, que integró la exposición de el(la) estudiante sobre el contenido de la misma y las preguntas formuladas por los miembros del Tribunal, se califica la sustentación del trabajo de titulación con las siguientes calificaciones:

Tipo	Docente	Calificación
Miembro Tribunal De Defensa	Dr. PINEDA ORDOÑEZ, LUIS EDUARDO , Ph.D.	9,2
Presidente Tribunal De Defensa	Dr. TORO ALAVA, JORGE EDUARDO , Ph.D.	8,9
Tutor	Dra. PIISPA , ELISA JOHANNA , Ph.D.	9,7

Lo que da un promedio de: **9.3 (Nueve punto Tres)**, sobre 10 (diez), equivalente a: **APROBADO**

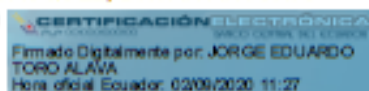
Para constancia de lo actuado, firman los miembros del Tribunal Calificador, el(la) estudiante y el(la) secretario ad-hoc.

Certifico que en cumplimiento del Decreto Ejecutivo 1017 de 16 de marzo de 2020, la defensa de trabajo de titulación (o examen de grado modalidad teórico práctica) se realizó vía virtual, por lo que las firmas de los miembros del Tribunal de Defensa de Grado, constan en forma digital.

Bryan Chamba 2020.11.20 14:20:05
-07'00'

CHAMBA VASQUEZ, BRYAN ANTONIO

Estudiante



Dr. TORO ALAVA, JORGE EDUARDO , Ph.D.

Presidente Tribunal de Defensa

ELISA JOHANNA PIISPA

2020.09.02 12:49:56 -05'00'

Dra. PIISPA , ELISA JOHANNA , Ph.D.

Tutor

LUIS EDUARDO PINEDA
ORDONEZ
PINEDA ORDONEZ
2 020 09 02 1154 35
-CS 107

Dr. PINEDA ORDONEZ, LUIS EDUARDO , Ph.D.
Miembro No Tutor


ANDREA YOLANDA
TERAN ROSALES
2 020 09 02 1154 35
-CS 107

TERÁN ROSALES, ANDREA YOLANDA
Secretario Ad-hoc

AUTORÍA

Yo, **Bryan Antonio Chamba Vásquez**, con cédula de identidad 1717876856, declaro que las ideas, juicios, valoraciones, interpretaciones, consultas bibliográficas, definiciones y conceptualizaciones expuestas en el presente trabajo; así como, los procedimientos y herramientas utilizadas en la investigación, son de absoluta responsabilidad de el/la autor (a) del trabajo de integración curricular. Así mismo, me acojo a los reglamentos internos de la Universidad de Investigación de Tecnología Experimental Yachay.

Uruguay, septiembre del 2020.

**Bryan
Chamba**  Firmado digitalmente
por Bryan Chamba
Fecha: 2020.11.23
19:59:12 -07'00'

Bryan Antonio Chamba Vásquez

CI: 1717876856

AUTORIZACIÓN DE PUBLICACIÓN

Yo, **Bryan Antonio Chamba Vásquez**, con cédula de identidad 1717876856, cedo a la Universidad de Tecnología Experimental Yachay, los derechos de publicación de la presente obra, sin que deba haber un reconocimiento económico por este concepto. Declaro además que el texto del presente trabajo de titulación no podrá ser cedido a ninguna empresa editorial para su publicación u otros fines, sin contar previamente con la autorización escrita de la Universidad.

Asimismo, autorizo a la Universidad que realice la digitalización y publicación de este trabajo de integración curricular en el repositorio virtual, de conformidad a lo dispuesto en el Art. 144 de la Ley Orgánica de Educación Superior.

Urcuquí, septiembre del 2020.

**Bryan
Chamba**  Firmado digitalmente
por Bryan Chamba
Fecha: 2020.11.23
19:59:32 -07'00'

Bryan Antonio Chamba Vásquez

CI: 1717876856

Dedicatoria

Las gracias totales a mi enorme familia, ustedes son la brújula que me guía, la inspiración para volar hacia grandes alturas y el apoyo cuando se presentan caídas.

No hay duda que este trabajo es dedicado a mis padres: Wilson Chamba y Piedad Vásquez, volver a nuestro hogar después de 5 años, me hicieron recordar que siempre volveré a los lugares donde amo la vida, y es ahí donde están mis padres.

Y finalmente, dedicado a mis herman@s, apoyo incondicional, guiando mi vida, reflejándome en sus logros. A mi hermano mayor, Fabricio, gracias por enseñarme el amor al trabajo. A mi older sister, Silvi (mi segunda madre), no tengo palabras para expresar el amor que te tengo y la gratitud total. A Cristinita, quien dio alegría a la familia, con Nicolás, muchas gracias por permitirme ser un ejemplo para mi sobrino. A mi gemelo Ronald, quien ha estado conmigo desde el primer milisegundo de mi vida, y sé que siempre estará ahí, gracias por ser mi mejor amigo. Al más pequeño Sebas, con quien entendí la importancia de ser un buen ejemplo, todo lo que hago es por ti y para ti.

VALIENTE Y ESFORZADO

Bryan Antonio Chamba Vásquez

Acknowledgements

This work is the proof of how the cooperation between communities and universities can reach excellent results. For this reason, the authors want to highlight the collaboration of Tamia Yura community on this research. Furthermore, authors thank everybody who form part of the the data collection. Along these years, many people helped us in the data collection, working in the middle of the jungle, under extreme weather conditions and during extensive labor journeys. I have no word to express my gratefulness, thank you Yachay Tech geology faculty and Rikuna Project. Finally, I would like to express my total gratitude to Elisa Piispa, her advice and collaboration shaped my scientific career. I learned to much from her experience.

Bryan Antonio Chamba Vásquez

Resumen

La presencia de rocas carbonatadas y los altos niveles de precipitación han llevado a la formación ubicua de cuevas kársticas en la región de Napo, región de la Amazonia en el noreste del Ecuador, parte central de la Zona Subandina (SAZ) oriental del Ecuador. Cuevas como estas representan un objeto científico importante, ya que suelen ser adecuadas para estudios estratigráficos, geofísicos, geoquímicos y paleoclimáticos. Trabajos anteriores han demostrado que los estudios de resistividad eléctrica son una manera muy eficiente y apropiada de detectar y definir cuevas poco profundas. Sin embargo, no se han realizado estudios de este tipo en cuevas ecuatorianas. A continuación, presentamos el primer estudio de este tipo en Ecuador. Nosotros mostramos los resultados de la aplicación de la técnica de tomografía de resistividad eléctrica (ERT) para caracterizar la cueva Uctu Iji Changa en la provincia de Napo, Tena, Ecuador. En general, los resultados coincidieron entre sí, y juntos señalaron tres capas geológicas: (1) una capa superior de ~ 2 a 9 m de espesor ($<50 \Omega\text{m}$ - piedra caliza); (2) una capa intermedia de ~ 2 a 4 m de espesor ($51\text{-}80 \Omega\text{m}$ - marga), donde nuestra atención se centra en la detección de cuevas; (3) otra intercalación de piedra caliza ($<50 \Omega\text{m}$); y una anomalía de alta resistencia ($80 > 100 \Omega\text{m}$), relacionada con las señales de la cueva. El estudio de ERT fue corroborado por inspección espeleológica dentro de la cueva. La ERT nos permitió determinar la ubicación y geometría general de la cueva y evaluar la precisión del método para detectar cuevas poco profundas en el sistema kárstico amazónico. En la mayoría de los perfiles, el contraste de resistividad entre las cavidades llenas de aire de la cueva y la cama de roca es lo suficientemente alto como para definir la ubicación de cuevas. Los resultados de este estudio resaltan que una modificación de la separación de electrodos en la configuración Dipolo - Dipolo es crítica para la identificación adecuada de cuevas poco profundas. Nuestros resultados demuestran la eficacia de la técnica de ERT para la detección de cuevas poco profundas asociadas con procesos kársticos.

Palabras clave: Resistividad eléctrica, cuevas kársticas, espeleología y provincia del Napo.

Abstract

The presence of carbonate rocks and high levels of precipitation have led to the ubiquitous formation of karstic caves in the Napo, region of Amazon in northeastern Ecuador, central part of the Subandean Zone. Caves such as these represent an important scientific target as they are typically well-suited for stratigraphical, geophysical, geochemical, and paleoclimate studies. Previous works have shown that resistivity surveys are a very efficient and appropriate way to detect and define shallow caves. However, no studies of this type have been conducted on Ecuadorian caves. Here, we present the first study of this kind from Ecuador. We show the results of applying the electrical resistivity tomography (ERT) technique to characterize the Uctu Iji Changa cave in the Napo province, Tena, Ecuador. The results from 13 survey lines show similar features pointing out three geologic layers: (1) a top layer of ~2 to 9-m-thick ($< 50 \Omega\text{m}$ - limestone); (2) a middle layer of ~2 to 4-m-thick ($51\text{--}80 \Omega\text{m}$ - marlstone), where our attention is focused for cave detection; (3) another limestone intercalation ($< 50 \Omega\text{m}$); and a high-resistive anomaly ($80 - >100 \Omega\text{m}$), related to signal from the cave. The ERT study was corroborated by speleological inspection of the cave to verify the results from the geophysical surveys. The ERT allowed us to determine the location and general geometry of the cave and to evaluate the accuracy of the method to determine shallow caves within the Amazon Karst System. In most survey lines, the resistivity contrast between the air-filled voids of the cave and the bedrock is high enough to define the approximate location and shape of the cavity. Our results demonstrate the efficacy of the ERT technique for the detection of shallow caves associated with karstic processes.

Keywords: Electrical Resistivity Tomography, karstic caves, speleology and Napo province.

Abbreviations

UICC: Uctu Iji Changa Cave

AKS: Amazon Karst System

ERT: Electrical Resistivity Tomography

AB: Amazon Basin

OB: Oriente Basin

GPR: Ground-penetrating Radar

RMS: Root Mean Square

SAZ: Subandean Zone

R: Resistivity

V: Voltage

I: Electrical current

J: Current density

E: Electrical field

r: Distance

ρ : Resistivity

Z: Earth impedance

K: Geometric factor

a: Distance between the pair of the current electrodes and potential electrodes

L: Distance between the centers of the two electrode pairs

A, B: Current electrodes

C, D: Potential electrodes

TABLE OF CONTENTS

TABLE OF CONTENTS	XVIII
CHAPTER 1 INTRODUCTION	1
1.1 STUDY AREA AND CAVE FEATURES	3
1.2 SOIL TYPE.....	4
1.3 CLIMATE	5
1.4 GEOLOGICAL SETTING	6
1.5 KARSTIFICATION.....	6
CHAPTER 2 PROBLEM STATEMENT.....	9
2.1 LOCAL PROBLEM STATEMENT	9
2.2 REGIONAL PROBLEM STATEMENT.....	10
CHAPTER 3 OBJECTIVES	11
CHAPTER 4 METHODS.....	12
4.1 STRATIGRAPHY OF THE CAVE	12
4.2 SPELEOLOGY	12
4.2.1 <i>Cave Safety</i>	13
4.3 ELECTRICAL RESISTIVITY.....	13
4.3.1 <i>Fundamentals</i>	14
4.3.2 <i>Equipment</i>	17
4.3.3 <i>Data Acquisition</i>	18
4.3.4 <i>Inversion of Dipole-Dipole Resistivity Data</i>	20
4.4 DATA PROCESSING	21
CHAPTER 5 RESULTS	25
5.1 MODEL OF FORMATION AND STRATIGRAPHIC COLUMN	25
5.2 ELECTRICAL RESISTIVITY SECTIONS.....	27
CHAPTER 6 DISCUSSION.....	38
CHAPTER 7 CONCLUSIONS	43
CHAPTER 8 FUTURE WORK AND RECOMMENDATIONS	44
ANNEXES.....	45
ANNEX 1	45
ANNEX 2	47
1) <i>ERT profile 4</i>	47
2) <i>ERT profile 5</i>	48
3) <i>ERT profiles 12</i>	49
REFERENCES.....	50

Chapter 1 Introduction

Caves are geomorphological structures defined as open space in the underground that can be free, full or partly water-filled or filled with other material (Putiška et al., 2012). Caves are formed in various ways such as through tectonic activity, lithostatic pressure, water erosion and chemical activity. Caves are typically classified in groups according to their genesis: (a) Volcanic caves: formed when lava flows get cold in their outer parts, while the interior part of the lava is still hot and moving; (b) Glacier caves: created due to the melting of the glacier's surface, creating a moulin; (c) Tectonic caves: result from fractures created by stress and strain; and (d) Limestone caves: molded by dissolution of bedrock due to groundwater flow. For this latter process, it is necessary the availability of soluble rocks and acid water (Davies & Morgan, 1987).

The Oriente Basin (OB) in Ecuador is the host of a big amount of limestone caves or karst caves, called the Amazon Karst System (AKS). The AKS was formed due to high hydric resources of the zone that penetrates the limestone surface with the help of cracks and diachases, creating an erosive agent that allows the formation of caves. The development of caves is intensified by the presence of acidic water. Carbonic acid is the most common acid in water due to the high abundance of carbon in the environment. The carbon dioxide (CO_2) that is present in the soil, organic matter and the atmosphere, is mixing with the water (H_2O) producing carbonic acid (H_2CO_3) (Frisia & Borsato, 2010).

AKS accounts for 5% to 10% of the total Ecuadorian surface, but most of it is still unexplored (Constantin et al., 2019). There are only few studies carried out in AKS that have a geological approach. Only a couple speleological, geochemical, and environmental characterization studies of the AKS exist (Bastidas, 2019; Debut et al., 2015; Padilla et al., 2015; Pemberthy, 2019; Toulkeridis et al., 2015a; Toulkeridis et al., 2015b). A good example of this, is the Uctu Iji Changa Cave (UICC) which is a limestone cave, located in the central Subandean Zone (SAZ) of Ecuador, that forms part of the AKS. Few caving explorations have been performed in this cave, but no geophysical characterization of it has been performed in order to locate the cave from the surface.

A geophysical characterization should be done in UICC and generally in the AKS. Geophysical surveys have demonstrated to be an effective instrument to detect the

proportions of cavities and to evaluate the level of vulnerability of these caves (Sciotti, 1982). Different geophysical methods can be used for detection of subsurface geomorphological structures.

- (a) Microgravimetry: is an example of geophysical technique that can be used to detect both natural and artificial caves (McDonald & Davies, 2003). The restriction of this method is when there is high ambient noise, which reduces the accuracy of measurements, especially in surveys conducted in urban areas. In our case, the noise created by the groundwater flow would decrease the precision of this technique. Furthermore, the high cost of this equipment was another limiting factor for the purpose of this study.
- (b) Ground-penetrating radar (GPR): is another technique used especially when inadequate access to the research areas do not allow the use of equipment that requires lot of space (Benson, 1995) . The limitation for this method is that the depth of penetration is controlled by the soil features. If the soil is very conductive, the penetration depth is poor (Heiland, 1940). In our study area, the soil is often very conductive due to water saturation. Resulting geological characteristics of the subsoil do not allow complete penetration of electromagnetic waves through the subsurface. Furthermore, the cost of the equipment is again another restrictive factor for the use of this equipment.
- (c) For this type of problem, electrical resistivity tomography (ERT) method has been established to be a very effective tool for the characterization of cavities (Cardarelli et al., 2006).

As a summary, microgravimetry and GPR are methods that allow geologist to characterize caves but for our research the ERT method is superior because of the following advantages. For the detection of caves, ERT is the most common method used, because of its low cost, easiness of transportation in field and its efficiency to detect caves (Benson, 1995; Cardarelli et al., 2006; Gambetta et al., 2011; Ortega et al., 2010; Putiška et al., 2012). In general, ERT is a cheaper and more lightweight equipment than gravimeter or GPR. This advantage was even greater because the electrical resistivity equipment used in this research was a home-build equipment. The equipment is lighter to carry and easier to set-up in hard locations and conditions.

Furthermore, since there is a high resistivity contrast between the host rock, which is water saturated limestone (low resistivity) and the air-filled cavities (high resistivity), the efficiency of ERT is excellent (Martínez-Pagán et al., 2013). For these reasons, we have selected ERT survey to map the shallow subsurface features in the UICC.

1.1 Study Area and Cave Features

The Amazon Basin (AB) covers about 35.5 % of South American continent and is in part located in multiple countries such as Bolivia, Brazil, Colombia, Ecuador, Guyana, Peru, and Venezuela (Burke & Lytwyn, 1993). The OB is the Ecuadorian part of the AB. The present study has been carried out over the Napo province, which is a part of the OB (Figure 1a). Uctu Iji Changa cave is a carbonate karst cave, situated at 510 m above sea level (ASL), in the OB, near Tena (Figure 1a).

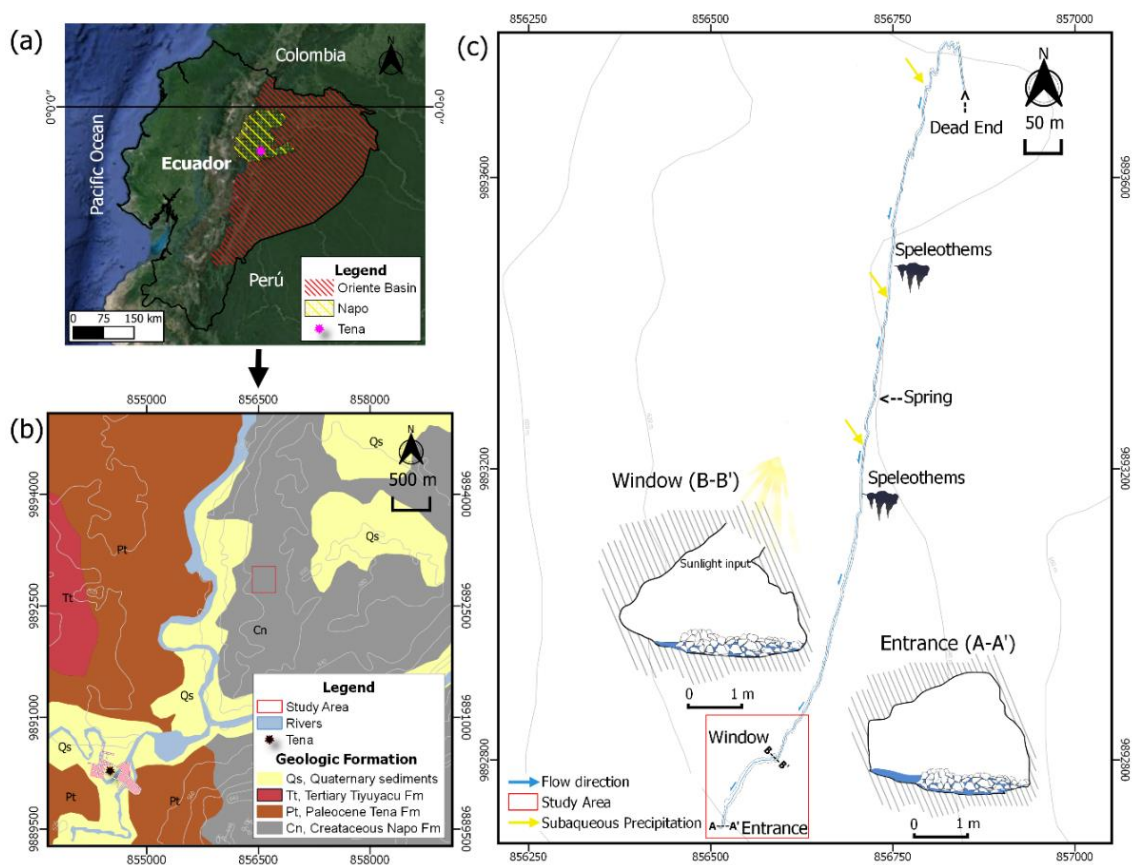


Figure 1. (a) General location of the study area in Ecuador showing the Oriente Basin region. (b) Geological map of the northwest Tena, UTM ZONE: 18M. (c) Map of the karst system Uctu Iji Changa Cave showing the water flow direction and two cross sections: at the entrance and at the window of the cave, UTM ZONE: 18M.

A part of the AKS is the Tena-Archidona region, which is characterized by shallow caves that rarely exceed 20 m depth. This occurs because the underground is composed by thin layers of limestones and interbedded shales that do not allow deep drainages. UIC is a natural cave located in the Tamia Yura community, which is 5 minutes northward from Tena city. It is a shallow cave with a 1174 meter long irregular path (Sánchez Cortez, 2017). Its maximum height is about 5.4 meter while its mean height is 2.6 meters. Its maximum width is about 7.9 meters while its mean width is 1.8 meters (Figure 1c).

The water resource of the UICC is defined by daily rainfalls which are quickly infiltrated in the vadose zone, and then this water is collected in the subsurface, either as creeks or as percolating water. There are no hydrological studies developed in UICC, but a drip water monitoring was carried out in the Jumandi cave during 6 months. Jumandi cave is 10 km from our studied cave, therefore we can use Jumandi's data to infer the water behavior in UICC. In Tena, the high level of precipitation creates fast fluctuations of groundwater flow rates, which are known to fluctuate as much as from 2 l/s to 2 m³/s within a few minutes (Constantin et al., 2019).

1.2 Soil Type

In tena city there are three types of soils: 1) Inceptisols, that are soils developed in previous sedimentary environments (sandstones and conglomerates), 2) Entisols, that are sedimentary soils developed in alluvial environments and 3) Histosols, that are volcanic soils, black in color and relatively fertile. Inceptisols represent the majority of the Tena city (73.88%) and is also the soil type where the UICC is located (Kléver, 2014). They are moderately new soils and are categorized by having the weakest appearance of horizons, or layers, produced by soil-forming factors. Their geographic settings are wide, from river to tundra environments. For example, they occur in the Mississippi valley, central Europe, Alaska, northeastern India and Amazon region (Foss et al., 1983).

The soils in the UICC are characterized by low agricultural productivity because the climate of the region allows the spread of pests and erosion. It is a type of soil characteristic of tropical regions, brown and reddish in color. At high depths, this soil is extremely acidic due to the high levels of aluminum and carbon dioxide. This determines

the poor chemical properties of the soils because this soil has a low cation exchange capacity (Gonzales et al., 1986).

1.3 Climate

The AB is one of the regions with the highest precipitation levels and a major evapotranspiration zone around the world (Manatsa et al., 2008). In order to show climatological information that corresponds to the study area, a spatio-temporal rainfall variability data at the Tena station is showed (Figure 2). The Tena city is located in a very humid hydrological regimen defined by persistent rains. This regimen is characterized to have an average annual rainfall of 3931,3 mm with an average monthly rainfall of 219 mm (Nouvelot et al., 1995). The 2019 interannual variability of total rainfall data at Tena Station are displayed in Figure 2. In the Tena city, the maximum rainfall (488 mm) was observed in June, while the driest month (258 mm) was in February. The total annual rainfall was 4330 mm in 2019. The temperature in Tena does not vary much through the year with an average temperature of 23,3 °C. The maximum temperature observed in 2019 was 23,8 °C in October while the minimum temperature registered was 22,6 °C in June.

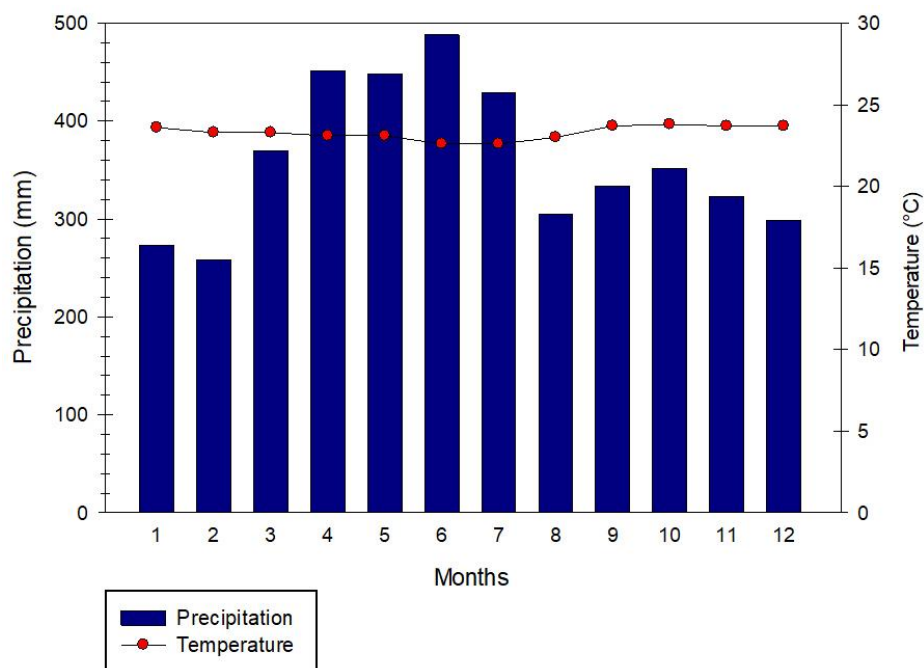


Figure 2. Interannual Climate Record of 2019 at Tena Station M5147. Source: (CLIMATE-DATA.ORG, 2019).

1.4 Geological Setting

The OB represents an area of approximately 100,000 km² and it comprises only the Ecuadorian part of the South American system of sedimentary basins. The formation of the basin started during the Late Cretaceous transgression (100.5 – 66 Ma), followed by the orogenic process of subduction that created the uplift of the Cordillera Real and the formation of the back-arc basin to the east (Dashwood & Abbotts, 1990). The study area is located in the Basal and Lower Napo Formations (Figure 1b) in terms of geology. The area is characterized by marine deposits of Upper Albian - Upper Cenomanian age (100.5 – 93.9 Ma), which are formed by sequences of sandstones, limestones and shales. The deposition of these cyclic sequences were controlled by eustatic processes generated in a low energy shallow-marine platform (Jaillard et al., 2005).

Two depositional stages are proposed for these marine deposits. Stage T sandstone interval: Sea level decreased in the late Albian (98 Ma) forming a sequence boundary and an erosive drainage network which subsequently was filled by incised valley sandstones during a transgressive process. Stage U sandstone interval: The sea level fell during the middle Cenomanian (94 Ma) creating another sequence boundary. This depositional stage represents the subsequent incised valley fill deposited during early transgression (White et al., 1995).

According to the geological setting, the stratigraphy in the UICC should be controlled by a sequence of sub-horizontal thin-bedded limestones with frequent occurrence of shale beds. The limestone of Napo Formation is frequently fossiliferous typically containing shells and also sometimes large ammonites.

1.5 Karstification

Karst environments develop in many locations around the globe, where limestones and dolomites crop out, and where there is sufficient amount of flowing water for the dissolution and weathering of carbonates. This contact between soluble rock and weathering by dissolution produces a unique suite of underground landforms normally dominated by subsurface drainage (Frisia & Borsato, 2010).

In the atmosphere, droplets and the CO₂ of the atmosphere combine to form an acidic solution. This solution then combines with soil CO₂ and produces a more efficient acid (Figure 3, soil zone).

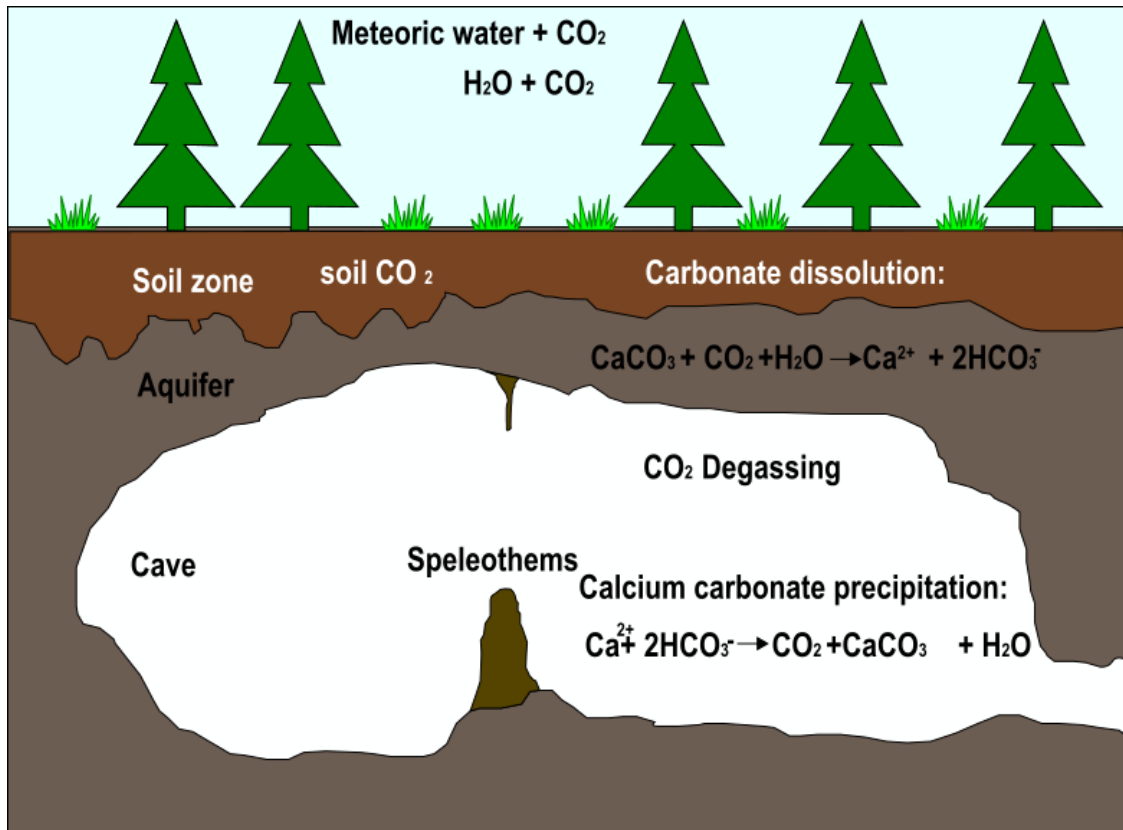
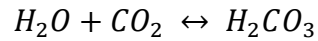
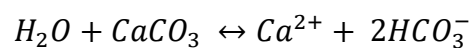
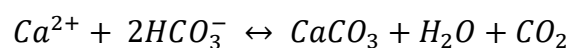


Figure 3. Schematic representation of the karst processes of dissolution and reprecipitation.

In the presence of acid water, calcite dissolution is much greater than in the presence of pure water. About 70% of dissolution is accomplished within the top 5 m and it diminishes with increasing depth from surface CO₂ supply (Figure 3, aquifer).



When the new solution is saturated of calcium carbonate and this solution enters the cave environment, a reprecipitation process occurs (Figure 3, speleothems). The reprecipitation of calcite is controlled by the reaction:



The reprecipitation process forms speleothems and CO₂ is released to the cave atmosphere. Degassing decreases the amount of CO₂ in solution, which becomes supersaturated with respect to CaCO₃. The droplet impacts with the speleothems growing from the cave floor and precipitates calcium carbonate at the tip of the speleothem.

Chapter 2 Problem Statement

2.1 Local Problem Statement

In the Ecuadorian Amazonian Region, the large-scale extraction of oil and the urbanization are affecting the areas inhabited by indigenous people. The changes that can result from these activities, increase vulnerability for indigenous communities because these affect their livelihoods (Bozigar et al., 2016). Tamia Yura is an Ecuadorian kichwa community, which has been largely affected by the modern world that has directly changed its ancestral way of life. For this reason, these people have had to adapt by using for example tourism as a way for activating their economy. In Tamia Yura, the main tourist attractions are hiking trails, wildlife sightings and cave exploration. By analyzing the situation of Tamia Yura community, we understood that the cave is of vital importance because it represents an economic support for them. Even though the immense significance of the cave for Tamia Yura community and their tourists, they still lack some essential information of the cave.

The knowledge that Tamia Yura has about the cave is attributed by empiric observations and by the research of Ikiam (Universidad Regional Amazónica). However, information on UICC is fragmented and contradictory. These two sources have marked differences regarding the dimensions of the cave and its projection on the surface, with different reported lengths or even locations. Considering the high level of vulnerability of Tamia Yura, and the relevance of the cave for the community, a geophysical characterization of the cave using ERT should be carried out to determine its real geomorphological features. This should be done in order to answer the following essential questions: (1) What is the length of the Cave? (2) What is both the max and min height-width? (3) How thick is the bedrock that covers the cave? and (4) Where is the cave path located on the surface? Answering these essential questions, we will be able to minimize potential risks (such as cave collapse, and related planning for paths and/or buildings on the surface, etc.) related to the cave for both the community and the tourism activity.

2.2 Regional Problem Statement

As it was mentioned in the introduction, very little is known about the karst environment in Ecuador. This limited knowledge can be explained by the following reasons. First, part of the country is in the Andean cordillera, where the main lithology is volcanic in origin (Constantin et al., 2019). Therefore, it is difficult to think that there are karst environments in Ecuador. Second, the AKS has not been studied much because of the dense vegetation that makes it difficult to access. In summary, the AKS has not been researched due to its limited geological abundance and its difficult accessibility. However, the oil industry has demonstrated that the problems of access can be overcome as long as there is an economic benefit. Therefore, it is clear that the AKS has not long been studied mainly due to economic factors.

In Ecuador, subsurface cavity detection is one of the main challenges of karst-related research. It is a really big problem for the nation because most of the known caverns have neither been explored nor projected on existing maps (Constantin et al., 2019). As mentioned before, the lack of research in the AKS is related to the availability of economic resources, therefore the lack of geophysical surveys in the AKS also is related to an economic factor. It is because geophysical survey equipments are typically exorbitantly high in cost, which prohibits their use in high scale. Therefore, in order to solve this urgent necessity, cheap geophysical equipment should be developed to explore the AKS in high resolution. We carried out a geophysical study using a homebuilt geoelectrical equipment in order to evaluate the reliability of ERT method to detect cavities in this environment.

Chapter 3 Objectives

Our study was conducted in a controlled environment in order to check its reliability in achieving the main goals: (a) to identify and characterize different geomorphological underground features, (b) to demonstrate the suitability of the ERT technique for characterization of shallow caves, (c) to evaluate the reliability of the ERT in detecting known shallow cavities, and d) to see whether the ERT method is able to mark any occurrences of new hidden cavities in the study area. Speleological exploration of the cave and its projection on the surface are the major geologic controls for the interpretation of the ER profiles of this study.

Chapter 4 Methods

The karst system Uctu Iji Changa Cave (UICC) was assessed on a multidisciplinary geological approach. The present study integrates several techniques: stratigraphy, speleology, and applied geophysics.

4.1 Stratigraphy of the Cave

In order to obtain the stratigraphy of the cave, we developed stratigraphic logs at two points inside the cave: The first point is located at the entrance of the cave, which is a room of approximately 1.90 m high by 3.20 m wide (Figure 1c, Entrance A-A'). The second point is located in the window of the cave, which is a room of approximately 2.5 – 3 m by 3 – 5 m wide (Figure 1c, Window B-B').

During the fieldwork, lithology, grain size, texture, sedimentary structures, contacts, color, geometry, paleocurrent directions, modal percentage, the relationship of the beds and the fossil content data was collected, analyzed and sketched. All of this information was summarized by stratigraphic logs.

Some physical characteristics of the bedrock were observed and/or measured directly in the field, the grain size was estimated using a comparative chart proposed by Chilingar (1956) for determining the size of the sedimentary particles. To identify the lithology and basic mineralogy of the beds HCl (Hydrogen chloride) and 10x hand lens were used. On the other hand, to establish the modal percentage of composition in each layer, we used the comparison chart for estimating percentage composition proposed by Terry et al. (1955).

Finally, the sedimentary structures, geometry and fossil content were identified through inspection in each one of analyzed beds and recorded in columns using proper symbology taken from literature.

4.2 Speleology

Cave surveying was done in order to describe the cartographic aspects of the UICC. In order to estimate the cave path and to record cave passage, the basic equipment used for speleology were employed: a) A *Brunton* compass, which is a compact pocket

instrument used for reading the magnetic bearing of a line; b) Measuring tape, which is a standard instrument used to measure length. We defined all cave passages according to changes in direction of the cave. This was the technique we employed to describe the cave. It means that a passage is defined until it changes in direction, then a new passage is defined. In total, 80 rooms were defined and each cave room was measured in terms of height, width, length and orientation. With this technique, a 3D model of the cave path was combining of the eighty 3D passages measured.

4.2.1 Cave Safety

In order for preparing to go caving , the team followed “A Guide to Responsible Caving” issued by the National Speleology Society (Jones, 2009). In summary, the management of safety while working in the cave was composed by the following rules:

- Safety first and always.
- Follow policies and have permits.
- Two experienced leaders all the time.
- Properly trained leaders.
- Leader at front and back of group.

Furthermore, the dangers of caving were defined in order to be prepared for them:

- Trips and falls
- Getting lost
- Dehydration
- Possible bad air and sickness
- Insects and or snakes biting.
- Rock fall
- Getting stuck
- Hypothermia
- Rainfall events

4.3 Electrical Resistivity

Electrical resistivity (ER) is a fundamental property of all materials including the earth’s subsurface, quantifying how strongly the subsurface opposes the conduction of electric current. It can be used for investigation of mineral deposits and geologic structures. This technique has been famous since the mid-1990s because of the rapid and reliable advancements in data acquisition, tomography modeling, and inversion techniques (Loke, 2000). This rapid advancement was stimulated by the exploration and discovery

of natural resources using geophysical methods. However, its application to cave exploration was slow because the commercial value of natural resources overshadows that of somewhat unprofitable natural caves. In recent years, this situation has changed due to the recognition of the advantages of the ER method for cavity detection. Today, many organizations and companies (tourism, construction) concerned with speleology employ ERT in order to detect shallow subsurface caves.

4.3.1 Fundamentals

Resistivity is a measure of the resistance (R) of a specific material to an electrical conduction with its units being called *ohm* [Ω] (Lowrie, 2007). Considering the Ohm's law, which states that the electrical current (I) through a material is equal to the voltage difference (V) across two points, we get:

$$V = IR \quad (1)$$

Laboratory investigations have showed that the longer the path the current needs to travel the larger the resistance. Furthermore, the resistance also varies with the cross-sectional area of the material, the larger the cross-section the smaller the resistance and vice versa (Lowrie & Fichtner, 2019). In conclusion, for a given material the resistance is proportional to the length (L) and inversely proportional to the cross-sectional area (A), as follows:

$$R = \rho \frac{L}{A} \quad (2)$$

Where ρ is the resistivity constant of the material with units of ohm - meters.

The quantities that are used to obtain the resistivity (R) are current (I) and voltage (V), from Eq. (1), i.e.: $R = V/I$. Since the electrical field is the change of potential divided by the change in length, i.e. : $E = -dU/dr = V/L$, and the subsurface current density is the current over the area, i.e. : $J = I/A$ we get an alternative form for the Ohm's law by rearranging and doing above substitutions for Eq. (2) (Todd & Mays, 2005).

$$E = \rho J \quad (3)$$

In the case of ground consider that an electric current (I) is injected in a surface with uniform resistivity. This current (I) will spread out spherically through the subsurface,

but only into the ground because the electric current cannot flow through air as air is considered a perfect insulator. Therefore, the current density (J) is equal to the electrical current (I) injected over a cross-sectional area (A) through which the current flows uniformly, where A is the area of a half sphere $2\pi r^2$.

$$J = \frac{I}{2\pi r^2} \quad (4)$$

Then, if we substitute J in in Eq. (3) we get an expression for the electric field (E) to be as:

$$E = \rho \frac{I}{2\pi r^2} \quad (5)$$

Voltage (V) is defined as work done by the electric field (E) on a moving test charge from infinity to a certain point. In other words, the voltage is then the integral of electric field (E).

$$V = \int_r^\infty E \, dr = \int_r^\infty \rho \frac{I}{2\pi r^2} \, dr$$

$$V = \rho \frac{I}{2\pi r} \quad (6)$$

Where r is the distance from the current source to the potential electrode. Eq. (6) was derived under the assumption that the subsurface has a uniform resistivity, but the resistivity distribution inside the Earth is heterogeneous in reality. It means that what we actually are finding with Eq. (6) is apparent resistivity (ρ_a). Re-arranging Eq. (6) to solve for an apparent resistivity gives:

$$\rho_a = \frac{V}{I} 2\pi r = Zk \quad (7)$$

Notice that the apparent resistivity can now be written as a product of the Earth's impedance $Z = V/I$ and a geometric factor (k), which in this case is $2\pi r$. The geometric factor (k) depends only on the arrangement of the current and potential electrodes. For geophysical prospection arrangements of four-electrode arrays are more commonly used and there are many types of four-electrodes arrays to choose from. The choice of the "best" array for a 2-D resistivity imaging depends on many parameters such as: the type of structure to be detected, background noise level, and sensitivity of the resistivity

meter (Loke, 2000). In practice, the most famous configurations are (a) Wenner, (b) Schlumberger, and (c) Dipole-Dipole.

In our study case, a dipole–dipole configuration has been selected for its advantages to obtain our goals: a faster data collection and its sensitivity to lateral variations in resistivity, i.e. it is excellent to detect caves or dikes (Putiška et al., 2012), as long as the survey is done perpendicular to the feature. This arrangement is composed of four electrodes, one electrode pair for measuring current and one electrode pair for potential (Figure 4). The distance between the pair of current electrodes, A-B, is given as “a” which is the same as the distance between the pair of potential electrodes C-D. Furthermore, the centers of the two pairs of electrodes are separated by a distance “L”.

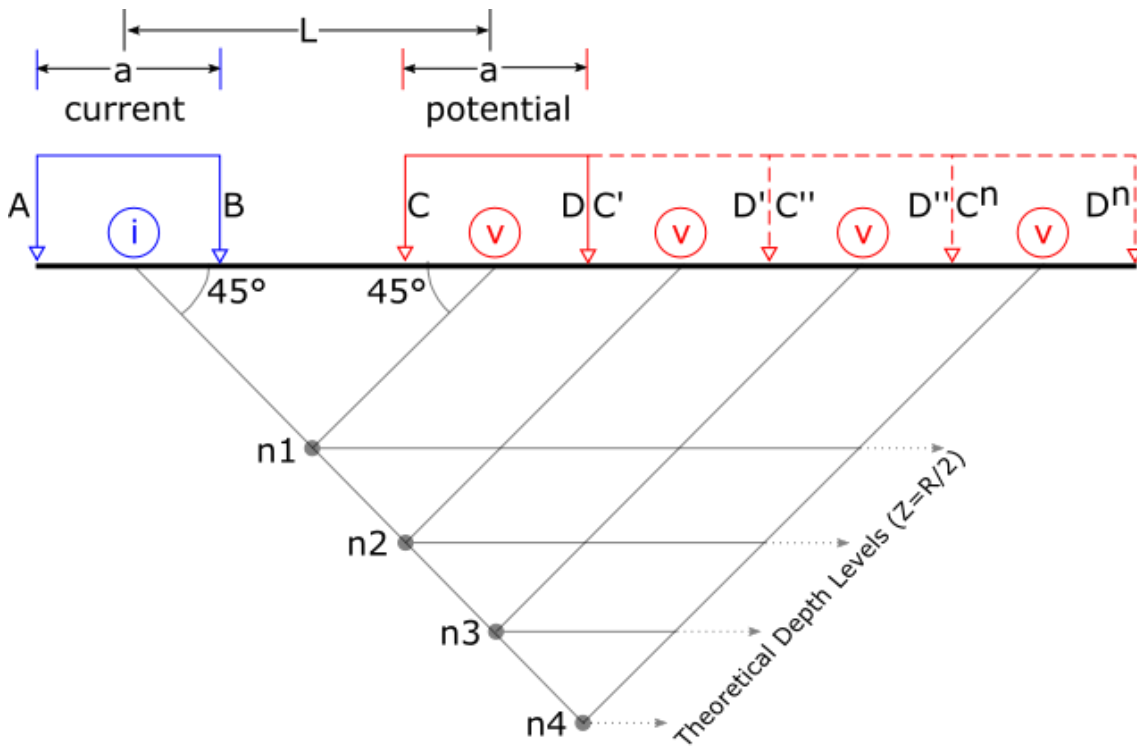


Figure 4. The dipole-dipole configuration showing the theoretical depth (also called apparent depth) reached when the current electrodes are moved laterally. Explanation of indexes: A, B current electrodes; C, D potential electrodes; (a) distance between the electrodes and (L) distance between the centers of the electrode pairs.

The geometric factor (K) for the typical dipole–dipole array is:

$$k = \frac{L(L^2 - a^2)}{2a^2} \quad (8)$$

The derivation for estimating this geometric factor is shown in Annex 1, part 1.

For surveys with this array, the position of current electrodes A-B and the “a” spacing are kept fixed. While the potential electrodes C-D are moved with a certain step size which is increased from C-D to C'-D' to C''-D'' until up to Cⁿ-Dⁿ in order to reach the desired investigation depth (Figure 4).

In order to reach deeper investigation depths, a modified dipole-dipole array was employed in the profiles 7 and 13. (see Table 1). For surveys with this modified array, the spacing between the current electrodes A-B is “a” while the spacing between the potential electrodes C-D is “b”. This modification in the electrodes spacing creates a modification in the geometric factor (k). The geometric factor for the modified dipole-dipole array is:

$$k = \frac{(2L - a_2)^2 - a_1^2}{3La_1a_2} \quad (9)$$

The derivation for estimating this geometric factor is shown in Annex 1, part 2.

The dipole-dipole configuration is susceptible to horizontal variations in resistivity, but comparatively insusceptible to vertical variations in the resistivity. Therefore, it is good in detecting vertical geomorphologies, such as dykes and caves, but comparatively bad in detecting horizontal geomorphologies such as sills or a sedimentary layer (Martínez-Pagán et al., 2013). The theoretical depth levels of this array are controlled by the distance between the centers of the electrode pairs “L” (Figure 4). For this reason, this array reaches shallower theoretical depth levels compared to some other arrays (Metwaly & Alfouzan, 2013).

4.3.2 Equipment

The ERT profiles were measured using an electrical resistivity equipment built by Dr. Elisa Piispa at the School of Earth Sciences, Energy and Environment of Yachay Tech based loosely on combining the works of Herman (2001) and Clark & Page (2011). It is an inexpensive equipment that was recently verified to give as reliable results as high-cost commercial resistivity equipment (Piispa 2020, personal communication). The homebuilt equipment is composed of: a power source (battery); a converter to convert 12 V direct current DC to 220 V alternating current AC; current electrodes (C1 & C2) to inject the current in the ground (e.g. 4 m long); potential electrodes (P1 & P2) to capture

the voltage (e.g. 4 m long), i.e. potential drop of the electric field; and two multimeters, one to measure the current in C1-C2 and the second to measure the voltage in P1-P2 (Figure 5).

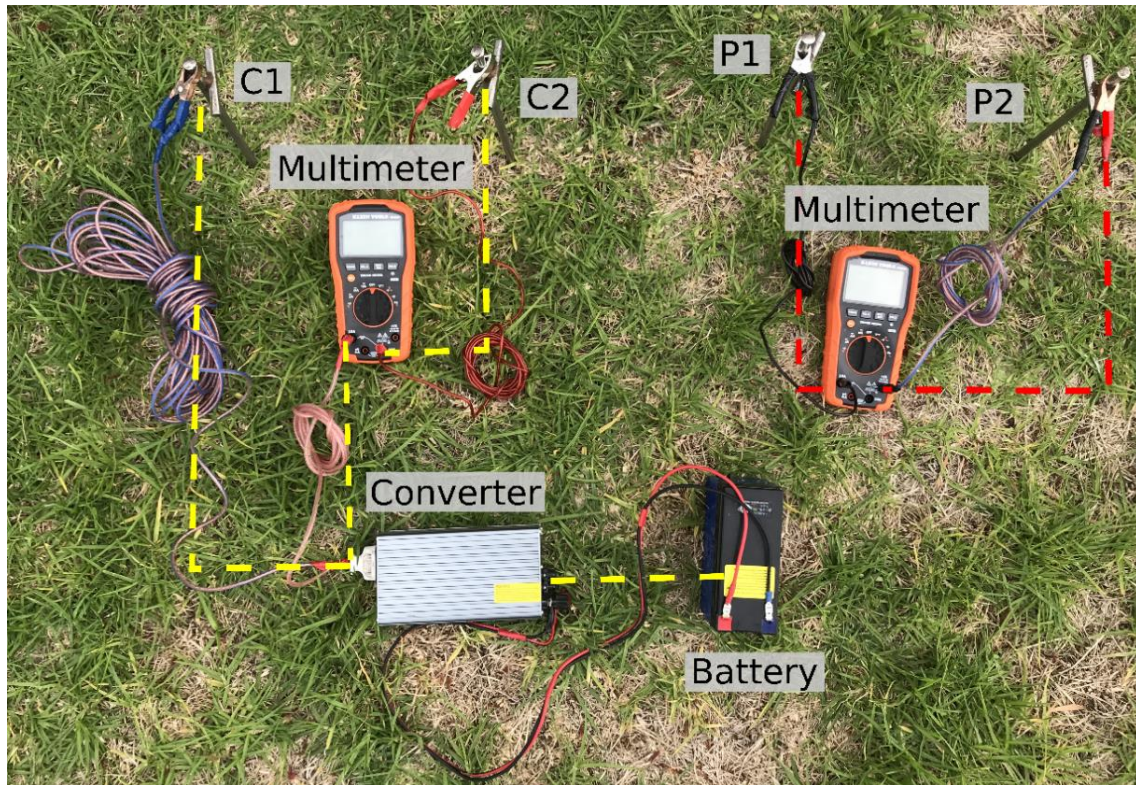


Figure 5. Homebuilt resistivity equipment with its components. Power source (battery), converter DC to AC, C1 & C2 current electrodes, P1 & P2 potential electrodes and multimeters. The electrodes are in a dipole-dipole array configuration. Image from Arteaga Pozo, (2019).

4.3.3 Data Acquisition

16 ERT profiles were carried out between "entrance-window" area of the cave, in the southmost side of the Uctu Iji Changa Cave (Figure 1). Two well-known underground rooms are located in this study area (the entrance and the window) and because we know the exact location of these in the surface, we chose this area to test the ERT technique in detecting shallow caves in the AKS. The 2D ERT data have been acquired along the most probable zones where the cave could be projected on the surface. The data acquisition plan was: (i) to choose profiles across or very close to a cavity feature, and (ii) to develop additional profiles through spots with similar geomorphology but unknown cave projection locations.

Four field trips were conducted in order to obtain 2D ERT data (Table 1). In the first field survey, only one ERT line of 28 m length was carried out. Nevertheless, after assessing the results of this survey line, it was clear that this line should be repeated, because of the length of this line was very short even for detecting the cave. To accomplish the goal of detecting the cave entrance, a second field survey was developed where the ERT profile 2 of 56 m in length was carried out in the same position as the ERT profile 1. Furthermore, in order to fully cover the area of the window cave, we laid out one parallel ERT profile 3 and one transversal ERT profile 4 (Figure 6). Once we had mapped the main underground rooms, two more ERT profiles (5 and 6) were laid out in order to cover zones very close to known underground rooms. Finally, a fourth field trip was developed to situate additional profiles through sites with similar geomorphological expression but with unknown projection of the cave in the surface. Profiles from 7 to 12 were carried out across the path entrance-window (Figure 6). Profiles 11, 12 and 13 were repeated profiles with data obtained starting from end of the line towards the start (reciprocal measurements) in order to test the reliability of the resistivity data. Technical parameters of all the ERT profiles are described in Table 1.

Table 1. Main characteristics of the ERT Profiles from UICC.

Field Trip	Date	ERT Profile	Orientation (° respect to North)	# of data points	Length (m)	“a” spacing (m)	Depth (m)	# of Iterations	RMS Error [%]
1	06/10/2018	1	82	30	28	4	5.9	6	1.9
2	07/12/2018	2	82	108	56	4	6.9	6	3.7
2	07/12/2018	3	350	96	50	4	6.9	6	2.8
2	08/12/2012	4	280	96	50	4	9.9	5	2.4
3	12/01/2019	5	335	98	48	4	9.9	7	19.2
3	12/01/2019	6	350	118	52	4	9.9	5	2.8
4	06/01/2020	7	315	240	70	4	12.2	7	3.5
4	06/01/2020	8	120	151	60	4	11.2	6	1.6
4	07/01/2020	9	320	140	60	4	9.2	6	2.3
4	07/01/2020	10	330	102	50	4	9.2	6	2.2
4	07/01/2020	11	320	102	50	4	9.2	9	2.8
4	08/01/2020	11'	140	102	50	4	9.2	5	3.5
4	08/01/2020	12	330	108	50	4	11.2	8	2.4
4	08/01/2020	12'	150	104	50	4	11.2	7	3.0
4	09/01/2020	13	320	204	70	4	11.2	5	8.1
4	09/01/2020	13'	140	208	70	4	11.2	6	3.7

Note. The ERT with the same number (11, 12, 13) are repeated because these ERT profiles were done from end to start of existing lines. RMS = Root Mean Square

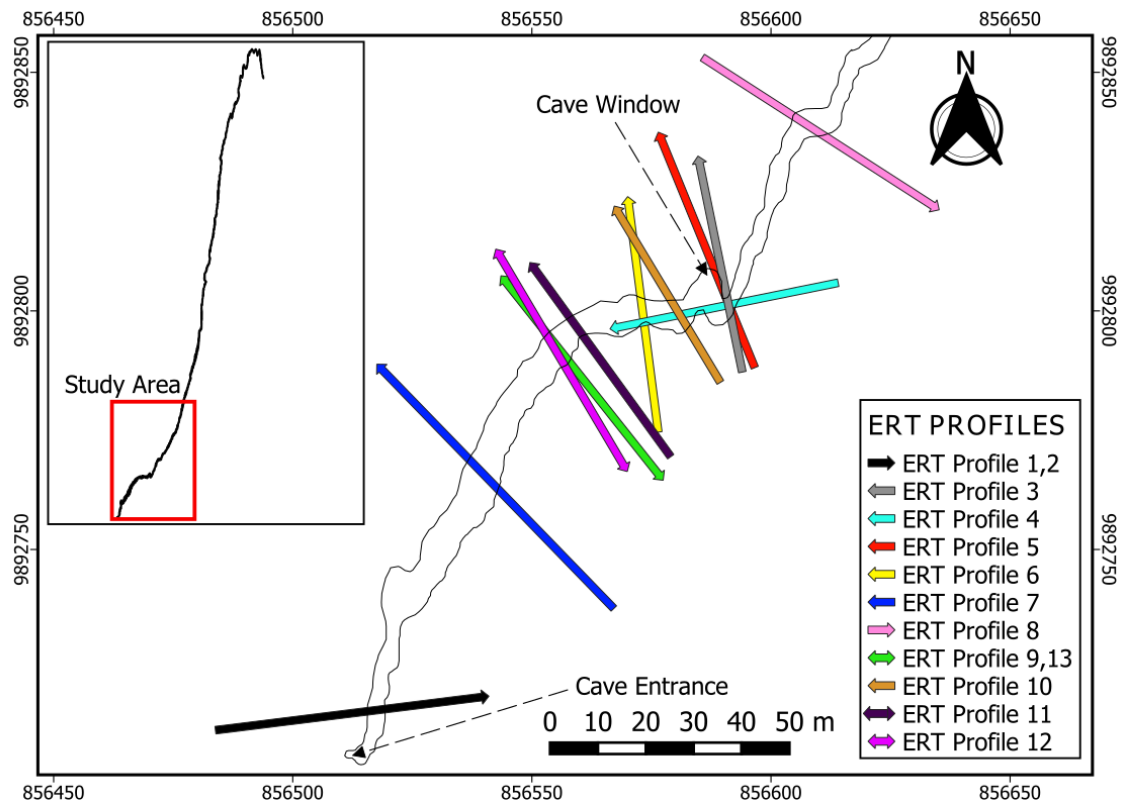


Figure 6. Subsurface map of Uctu Iji Changa Cave showing the collected ERT profiles. The arrow direction indicates in which direction the survey was conducted. In lines 11,12 and 13 the survey was done in both directions.

4.3.4 Inversion of Dipole-Dipole Resistivity Data

After the field surveys, the measured values of voltage and current were reduced to apparent resistivity readings using (Eq. 7) with the geometric factor (K) for the typical dipole–dipole array (Eq. 8). The apparent resistivities for the profiles 7 to 13 were calculated using the equation 7 with the geometric factor for the modified dipole–dipole array (Eq. 9). Practically, all commercial multi-electrode systems come with in-build computer software to carry out this conversion. However, our homebuilt equipment does not have a console to calculate automatically this value. For this reason, electrical measurements collected in the field from each profile were analyzed in a two-stage process: First, we used a specialized Excel sheet for initial data processing to calculate the apparent resistivity (ρ_a) values and include topography data; and following this stage, the apparent resistivity data were employed into an inversion procedure with RES2DINV software for generating 2D ERT models (Metwaly & Alfouzan, 2013).

In order to model using apparent resistivity, the RES2DINV software subdivides the underground into a number of blocks (Figure 7a), where its widths and heights are controlled by the spacing between adjacent electrodes (Loke et al., 2003). Then, the inversion technique “The regularized least-squares optimization method” determines an adequate resistivity value for each of the blocks (Figure 7b) (Sasaki, 1986).

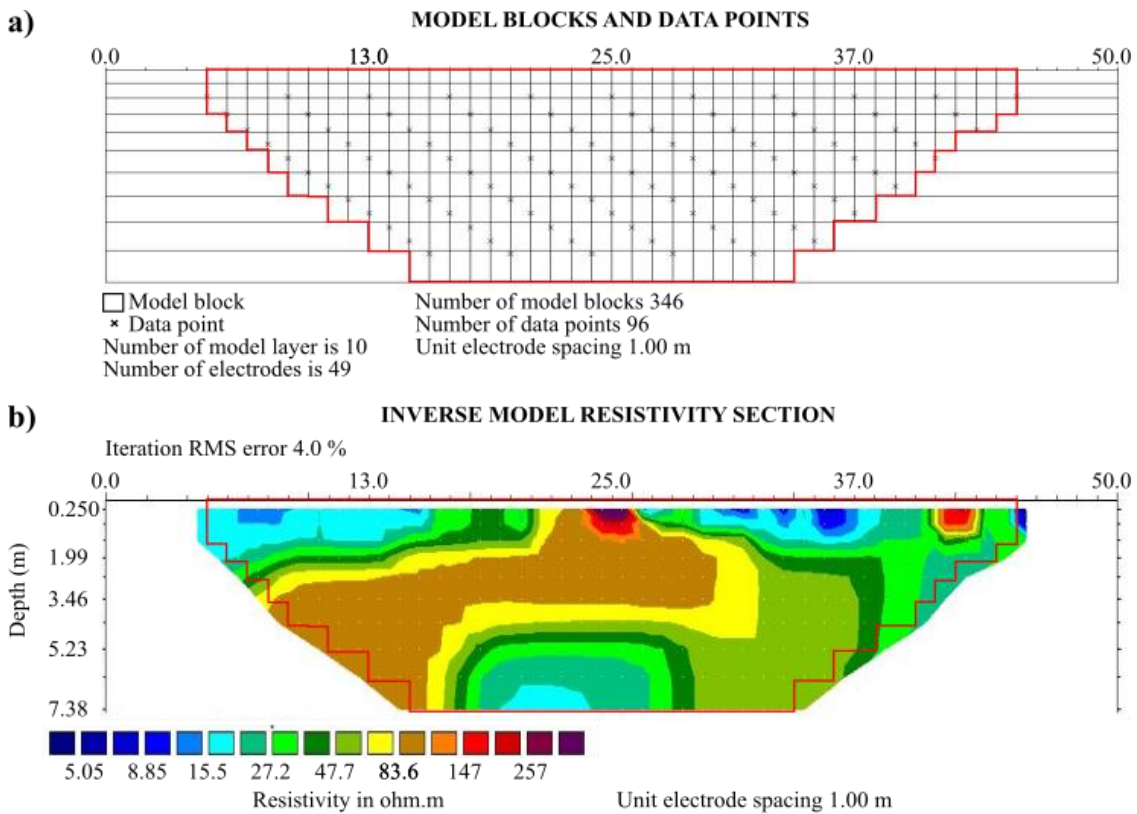


Figure 7. Fundamental concepts to carry out a 2D inverse model a) Arrangement of model blocks showing the ER data points. b) Inverse model resistivity section. The red line shows the relationship in space between the model blocks and the inverse model.

4.4 Data Processing

There is no unique processing procedure for resistivity data, instead there is a wide range of these to calculate an inversion model. To select the best processing routine, normally some assumptions are made concerning the nature of the subsurface and the selected array. In order to be able to adequately process the dipole-dipole resistivity data, the following processing technique was used based on the literature (Loke, 2000; Loke, 2006): First, the electrodes spacing and apparent resistivity values ought to be typed into a text file called “dipole-dipole.txt” that can be read by the RES2DINV program (Figure 8); Second, the inversion options must be modified in order to use a

model refinement. In the model blocks, the widths and heights of the blocks are controlled by the electrode spacing and it works well in most cases. Nevertheless, if there are large variations of resistivity near the surface, a narrower model block should be used (Loke, 2006). This inversion option is very important for the dipole-dipole array because it is more sensitive to shallow surface variation (Loke, 2006). For this reason, we use the approach, where the widths of the cells are set at half the spacing between adjacent electrodes.

Data file	Comments
DIPOLE-DIPOLE ARRAY	-->Name of the survey line
2	-->Unit electrode spacing "x"
11	-->General Array type, 11 for Dipole-Dipole
3	-->Subarray type, 3 for Dipole-Dipole
Type of measurement	
0	-->Type of measurement, 0 for apparent ER
318	-->Number of data points
2	-->X-location for data points, 2 for second electrode
0	-->Flag for I.P. data, 0 for none
4 0 0 4 0 6 0 10 0	447.480604
4 0 0 4 0 8 0 12 0	502.654825
4 0 0 4 0 10 0 14 0	431.576291
4 0 0 4 0 12 0 16 0	306.619443
4 0 0 4 0 14 0 18 0	222.660379
4 0 0 4 0 16 0 20 0	163.362818
C1(x) C1(z) C2(x) C2(z) P1(x) P1(z) P2(x) P2(z) Apparent Resistivity	

Figure 8. Example part of a data file Dipole-Dipole.txt that can be read by the RES2DIN.

Then, another factor that we can control is to exterminate bad data points. Erroneous data points are created by bad relay of the electrodes or poor electrode ground contact. These bad data points have typically apparent resistivity values that are too large or too small compared to the other surrounding data points (Loke, 2000). The bad points should be excluded so that they do not impact the inversion (Figure 9).

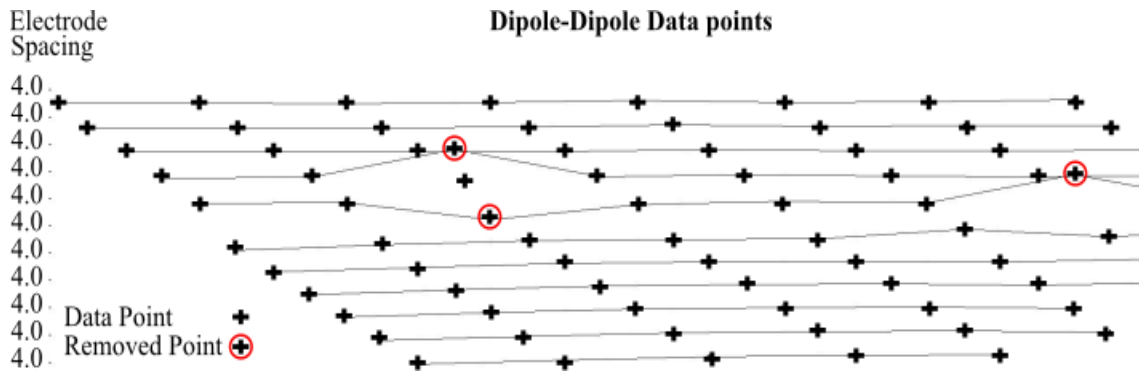


Figure 9. Example part of a data set with a few bad data points.

As a final step, the data outliers can be further filtered using the Root Mean Square (RMS) error statistics processing. RMS error calculates the data misfit between measured and calculated apparent resistivity values (Loke, 2006). Data outliers are likely to have much higher data misfit values which can be used to separate them from the other data points. In this option, the user selects a data misfit cutoff value (Figure 10).

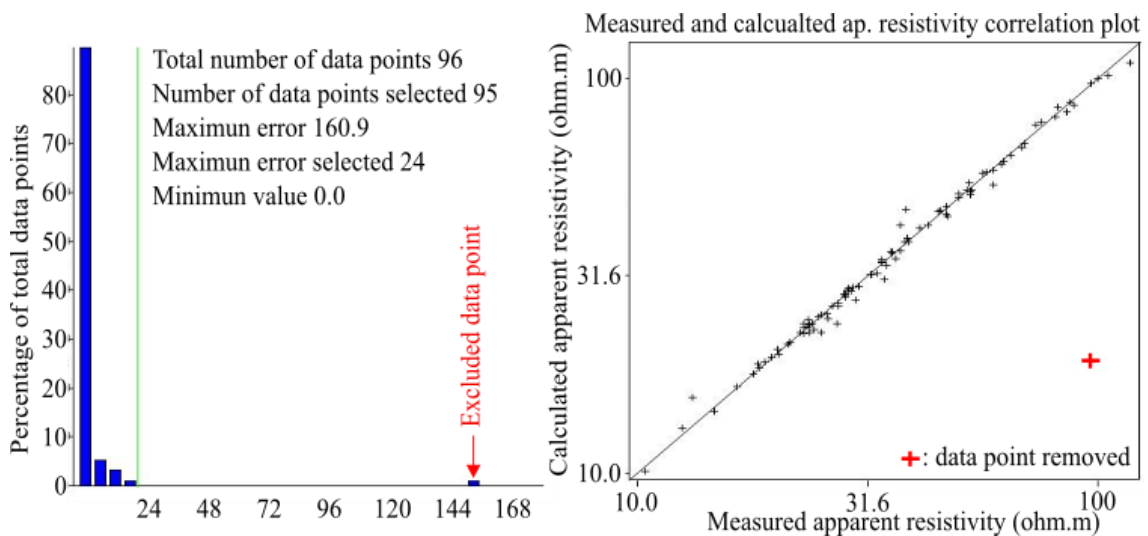


Figure 10. RMS error statistics showing data misfit between the measured and calculated apparent resistivity data.

In order to show the effect of our processing, a comparison between unprocessed and processed data is shown. The RMS error in the first model is 4.4 % while the RMS of the second model is 2.3 % (Figure 11). Both RMS errors are completely acceptable and the models are very similar, however, the second model reveals the resistivity variations better. With this example, we conclude that our processing routine will be successful to carry out the inversion process of our ERT profiles.

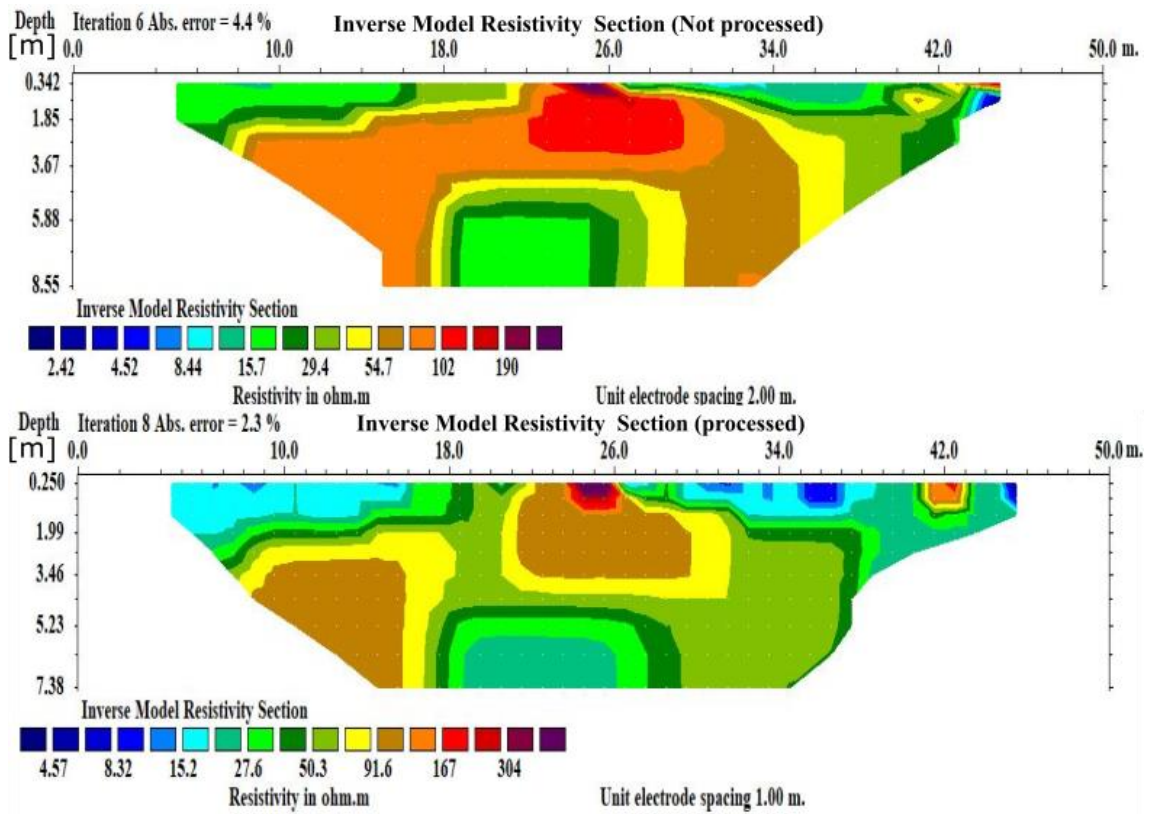


Figure 11. Example of the processing effect, above the un-processed inverse resistivity model and below the processed model as further explained in the text.

Chapter 5 Results

5.1 Model of Formation and Stratigraphic Column

As was mentioned in the introduction, the origin of the UICC is due to dissolution of the host rocks by acid water flow. However, it is important to understand that this process is not a random event, it is controlled by specific factors of the cave. These factors are: 1) limestones sediments and 2) the tectonic setting of the area. Figure 12a shows how the geomorphology of the cave was controlled by the weathering paths, which were able to percolate due to the joints and holes in the limestone rocks (Figure 12b). For this reason, developing a formation model and a stratigraphic column are crucial in order to understand the morphological evolution of UICC over time. The results of the stratigraphical characterization of the samples collected from UICC are presented and discussed.

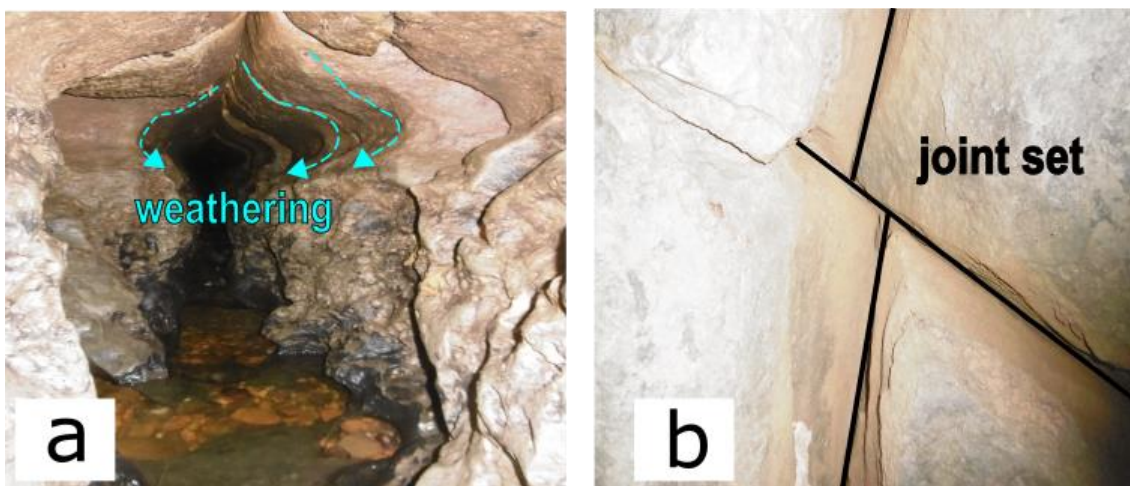


Figure 12. a) General geomorphology of the UICC showing the weathering paths (Light blue dashed arrows). b) Example of joints in the surface limestone where the water percolates.

The formation of the UICC can be explained by the following process, first the rainwater becomes slightly acidic from adsorbing carbon dioxide (CO_2) in the soil and the atmosphere (Figure 13a). Then this water percolates down along and adjacent to faults and cracks that were created by tectonic activity (Figure 13b). These openings are expanded by the dissolution of calcium carbonate (CaCO_3) in the rock, as well as abrasion as sediment is transported through them (Figure 13b). These openings allow the water flow to erode the marlstone creating the cave passages. Then, when the percolation

flow is saturated with CaCO_3 , CO_2 is degassed from the solution upon entering the cave and CaCO_3 is precipitated forming speleothems, drop by drop (Figure 13d). Finally, the cave passages are strictly limited to insoluble bioclastic limestone beds which act as a sub-horizontal boundary of the cave. It is because the water inside the cave is not acidic enough to dissolve the limestone floor (Figure 13e). As a general rule, in the UICC, the thinness of carbonate bedrock and presence of marlstone do not allow the formation of deep karstic rooms, and these rarely exceed 5 m height.

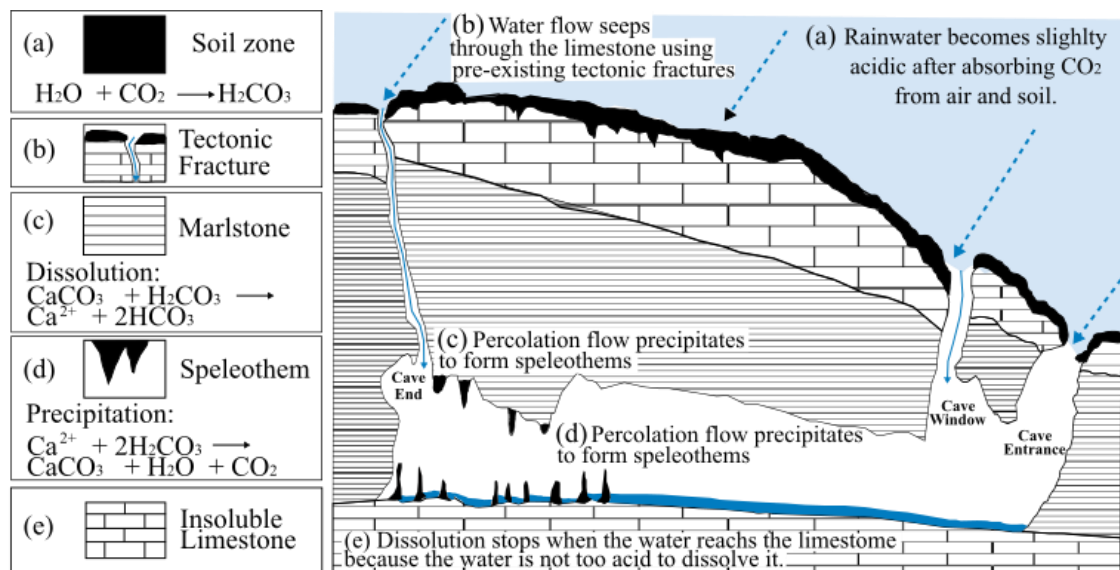


Figure 13. Schematic model of the formation of sub-horizontal Uctu Iji Changa Cave.

The stratigraphy of the UICC, from bottom to top, is composed by the following sequence:

1. Substratum (Floor): Very fine grained, grainstone, dark gray in color, very compacted and rich in fossil content (brachiopods).
 - Interpretation: Bioclastic limestone.
2. Cave passage: ~4 meters thick, very fine grained, marlstone, light gray in color, medium well compacted, with carbonate nodules 1 cm to 10 cm in diameter.
 - Interbedded: 0.2meters thick, very fine grain, mudstone, brown in color and poorly compacted.
 - Interpretation: Marlstone with interbedded mudstone beds.
3. Ceiling: Very fine grained, grainstone, dark gray in color, very compacted and rich in fossil content (brachiopods).
 - Interpretation: Bioclastic limestone.

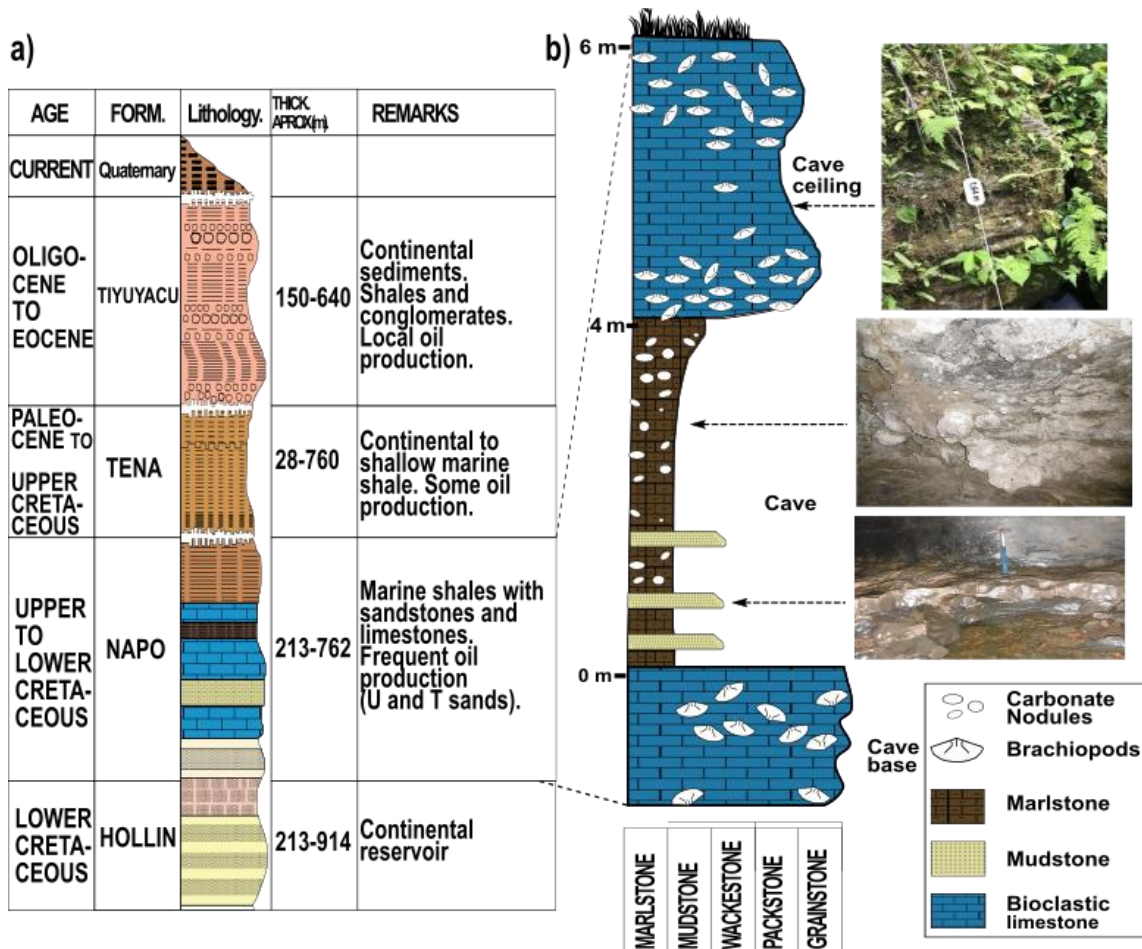


Figure 14. Stratigraphy of the study area. a) Generalized stratigraphic column for the Oriente Basin with lithostratigraphic nomenclature (modified from Almeida, 1986). b) Stratigraphic column of Uctu Iji Changa developed at the cave entrance.

Understanding the stratigraphy where the UICC is located, we infer that the cave belongs to one limestone sequence of the Napo Formation. However, with the information available, it is impossible to determine exactly in which limestone sequence from Napo Formation UICC belongs to.

5.2 Electrical Resistivity Sections

The inverted electrical resistivity sections allow us to distinguish three different units: 1) an upper one, that exhibits the lowest resistivity values; 2) a middle one, with the highest electrical resistivity; and 3) a lower one with similar resistivities as the first layer (Table 2). The middle layer is where our attention is mainly focused for the detection of the cave. Table 1 summarizes the mean characteristics of each ERT profile such as orientation, number of data points, length, electrode spacing, apparent depth, and RMS error. Profiles 4, 5 and 12 are not presented below because they are similar to other

profiles. However, these profiles and their interpretations can be found in the Annexes (Annex 2).

Table 2. Approximate resistivity ranges for the geological units in the UICC.

Geologic unit	Resistivity (Ωm)	Thickness (m)
Limestone	< 50	2 to 9
Marlstone	51 to 80	2 to 4
Superficial karstic cavities	81 to 100	2 to 4
Deeper karstic cavities	< 111	2 to 4

Note: Superficial cavities are cave rooms/cavities that have a connection to the surface and deeper cavities are rooms that are complete covered by limestone.

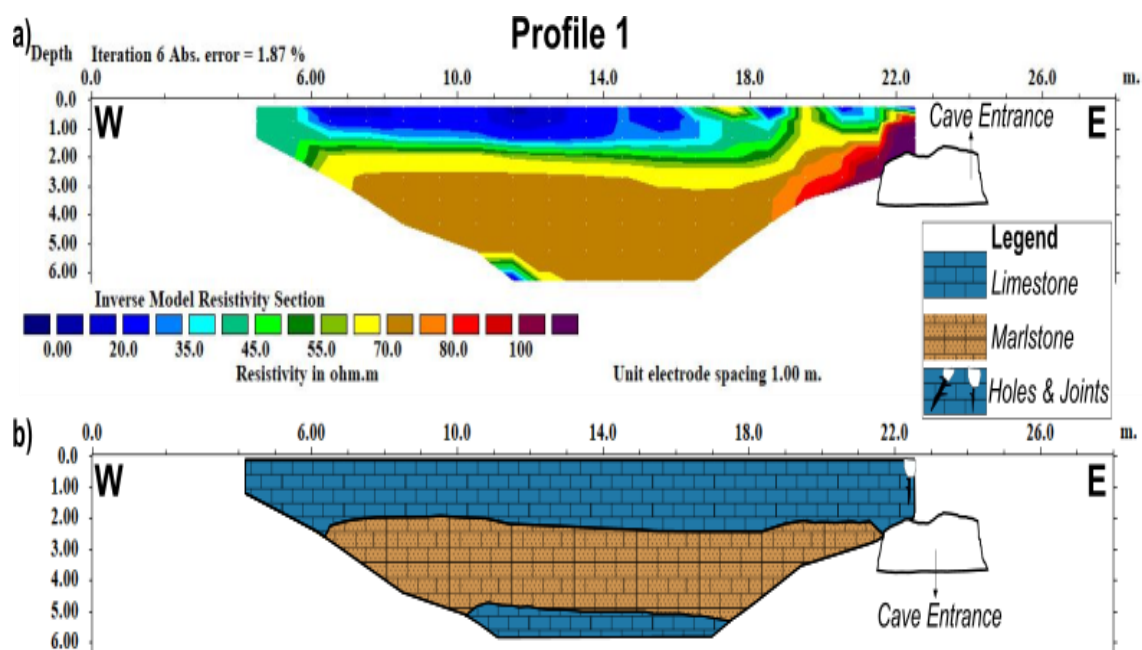


Figure 15. (a) Electrical resistivity section of the ERT profile 1, and (b) sketch of the interpretation of the subsurface geology and cavity model obtained through integration of ERT data and stratigraphy.

The profile 1 shows electrical resistivity patterns that are consistent with the rest of the processed ERT sections (Figure 15b). The shallowest layer is characterized by electrical resistivity values below $55 \Omega\text{m}$ with a maximum thickness of around 2 m. Underlying the shallowest unit, there is a second unit characterized by higher electrical resistivity values ($60 \Omega\text{m}$ to $75 \Omega\text{m}$), with a thickness of approximately 3 m from $x=0$ m to $x=19$ m showing a narrowing from $x=20$ m. At $x=22$ m, the highest electrical resistivity anomalies ($80 \Omega\text{m}$ to $>100 \Omega\text{m}$) display evidence of the cave (Figure 15b). Nevertheless, in this area the inadequate length of profile 1 prevented us from detecting the cave fully. Underlying the middle unit, there is a hint of a third unit characterized by lower electrical resistivity

values below 55 Ωm , and with undefined thickness because the ERT profile has a maximum pseudo depth of 5.9 m (Table 1), and therefore the survey does not reach to the bottom of this layer (Figure 15a).

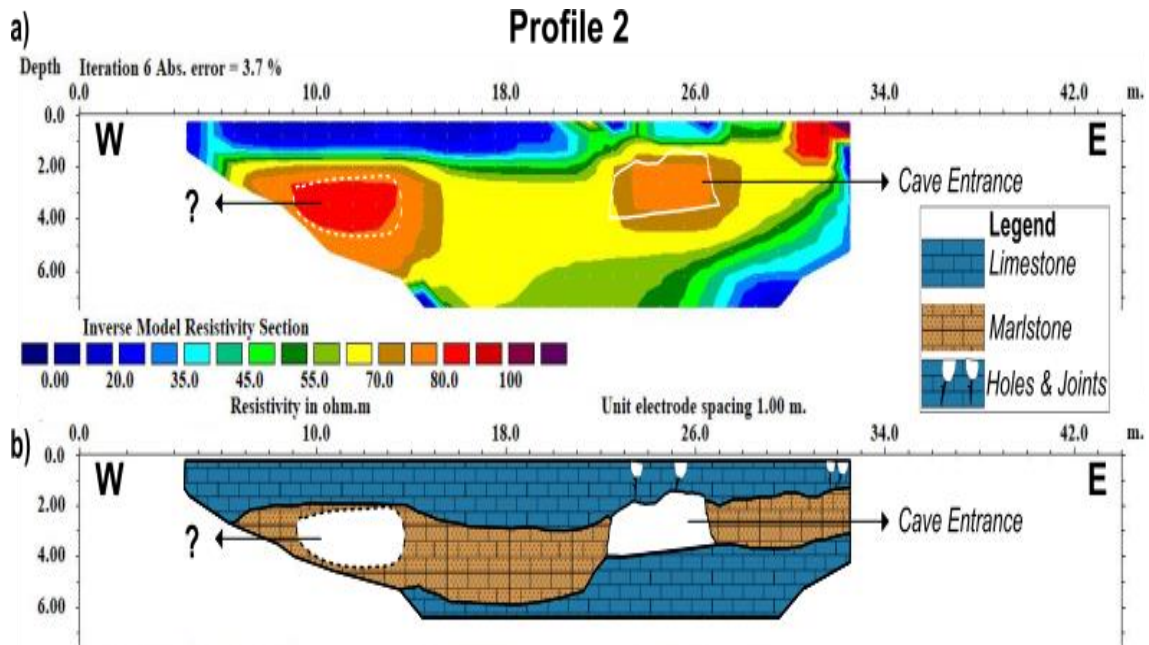


Figure 16. (a) Electrical resistivity section of the ERT profile 2, and (b) sketch of the interpretation of the subsurface geology and cavity model obtained through integration of ERT data and stratigraphy.

The ERT profile 2 (Figure 16a) shows the same resistivity layers as were described on Profile 1. The behavior of the top layer is almost identical to the first layer of Profile 1, but as this profile is longer, this layer shows a peak resistivity under position $x = 31$ m ($>100 \Omega\text{m}$). Due to superficial exploration along the profiles, the presence of big holes (~ 0.35 m wide) is reported here. The location of these holes correlates with this resistivity peak near the surface. The middle layer narrows rightward showing a minimum thickness of 2 m. On the left side, an unexpected oval-shaped resistivity anomaly is observed ($85 \Omega\text{m}$). This anomaly is labeled on the electrical section with a question mark, it could indicate an unidentified cavity (Figure 16b). On the right side, the position of the cave entrance has been outlined and it relates with an irregular resistivity anomaly with higher resistivity values ($80 \Omega\text{m}$). Finally, the bottom layers top moves towards the surface giving an impression of this layer thickening towards the right extreme corner of the electrical section.

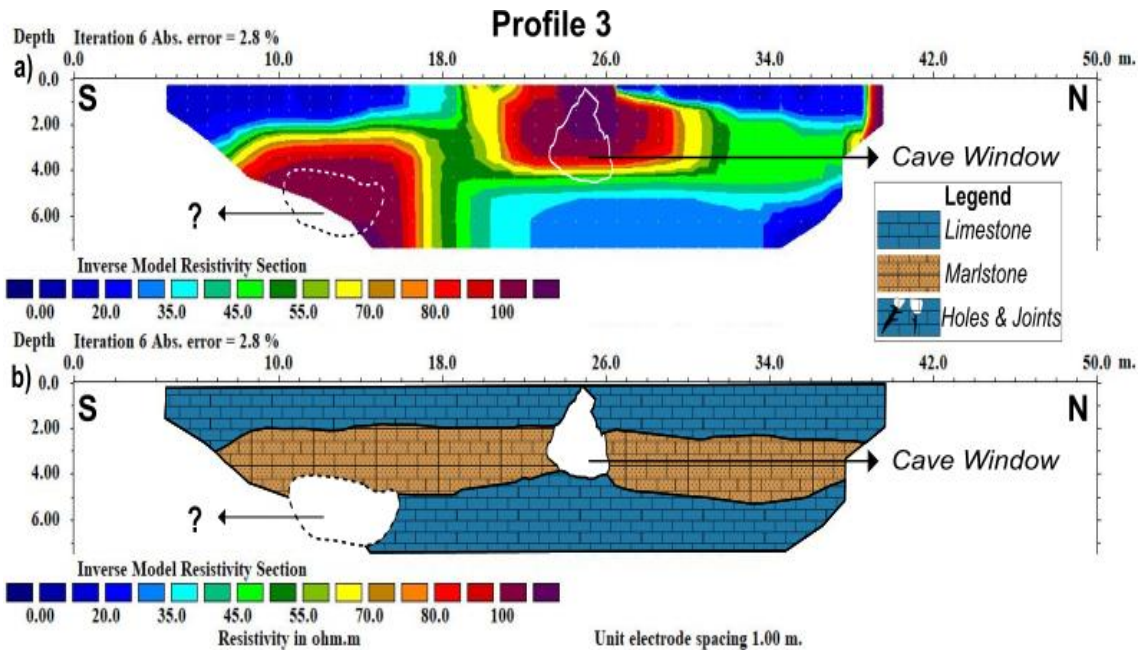


Figure 17. (a) Electrical resistivity section of the ERT profile 3, and (b) sketch of the interpretation of the subsurface geology and cavity model obtained through integration of ERT data and stratigraphy.

ERT profile 3 crosses perpendicularly the cave window (Figure 6). Its 2-D resistivity section has an upper layer with electrical resistivity values ranging from 10 Ωm to 55 Ωm and its thickness remains fairly constant (~ 3 m) through the profile (Figure 17). A second layer is characterized by electrical resistivity values ranging from 60 Ωm to 75 Ωm , which agrees with the electrical resistivity values of previous profiles. Inside this second layer are two high resistivity anomalies located under positions $x = 10$ m to 15 m and under $x = 20$ m to 27 m. These two resistivity anomalies reached values of >100 Ωm . The first anomaly was unexpected and could indicate another cavity that is not part of the main cave system (Figure 17b). The anomaly at ~ 25 m corresponds to the cave room underneath the window and correlates well with the data collected during the speleology (Figure 17b). For the deepest layer, the resistivity values are on the same range as the first layer and on the left side it is impossible to define the behavior of the strata due to the high resistivity anomaly covering the bottom of the model on this side.

In Figure 18a, ERT profile 6 displays three sub-horizontal units: the upper unit shows low resistivity values (< 55 Ωm) and its thickness is ~ 2 m for the first few meters thickening towards right (~ 4 m). A middle layer shows values ranging from 55 Ωm to 85 Ωm and its thickness is almost constant through the profile (~ 3 m). This layer shows an ovals shaped resistivity anomaly (>80 Ωm) that it is interpreted as signal of the cave (Figure 18b). This

anomaly has dimensions of ~5 m width to 3 m height, which matches extremely well with the measurements done inside the cave. In the bottom of profile 6, a third unit can be recognized showing again low resistivities below 50 Ω m. This unit is sub-horizontal dipping rightward. As in other profiles, due to the length of the profile, and the electrode configuration and ERT equipment used, we were not able to reach the bottom of this third unit.

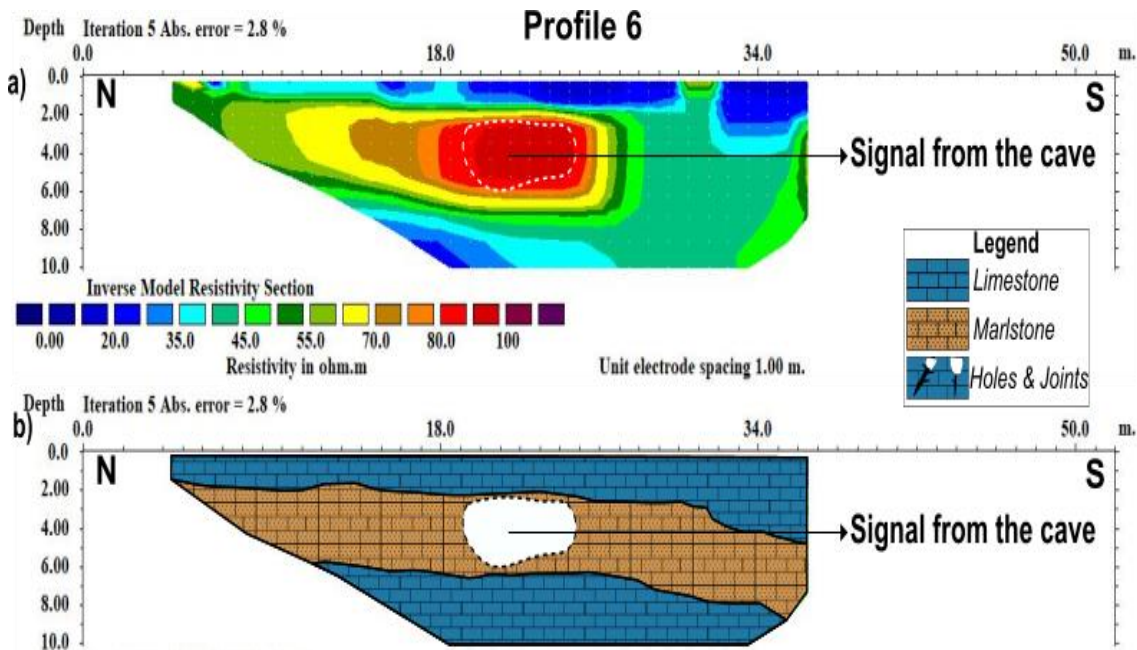


Figure 18. (a) Electrical resistivity section of the ERT profile 6, and (b) sketch of the interpretation of the subsurface geology and cavity model obtained through integration of ERT data and stratigraphy.

From profile 7 to profile 13, all the ERT profiles were developed in the last field trip and they were carried out over zones where the exact location of the cave is unknown. Furthermore, these profiles were done using a different electrode configuration, which gives us a new geometric factor (k). This new geometric factor allows us to reach deeper theoretical depths in order to try to detect a signal from the cave in locations where the cave is below a thicker overburden. The topography of these profiles was obtained analyzing slope variation during the data collection.

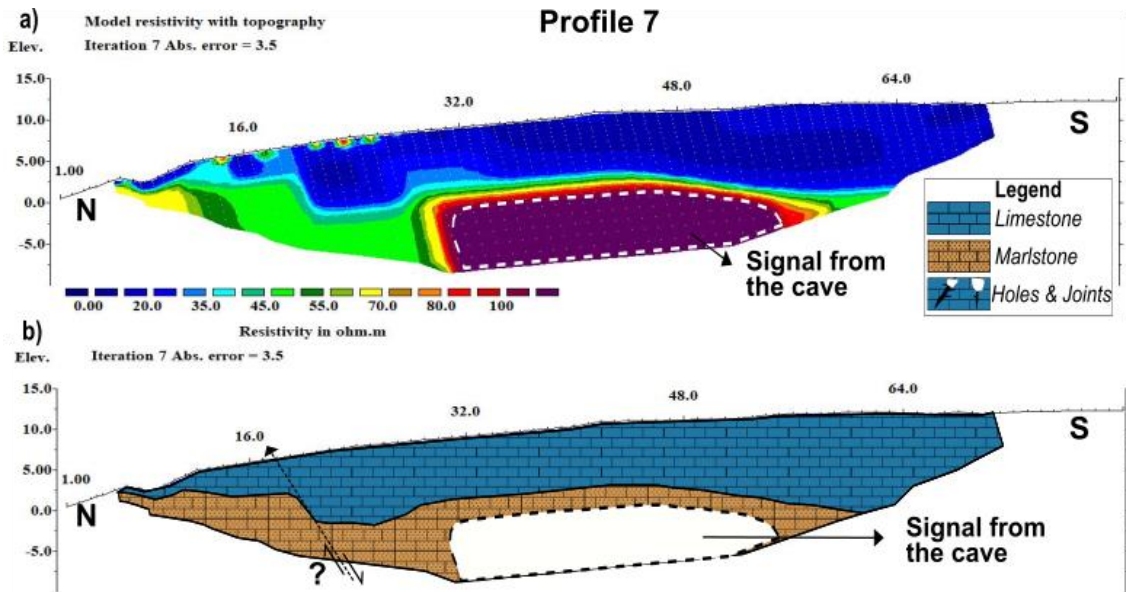


Figure 19. (a) Electrical resistivity section of the ERT profile 7, and (b) sketch of the interpretation of the subsurface geology and cavity model obtained through integration of ERT data and stratigraphy.

The electrical section 7 (Figure 19a) depicts two main resistivity regions; the upper layer has an electrical resistivity value ranging from 10 Ωm to 45 Ωm correlating well with the electrical resistivity values obtained for this layer through the previous six ERT profiles. The thickness of this layer changes in accordance with the topography, at the topographically lowest part of the profile, it is thinner, and at the right-hand corner, at the topographic high, it is thicker (~7 m thickness). The inverted electrical section ascertains that the upper layer is underlain by a more resistive region, with the strongest electrical resistivity anomalies encountered under the electrode positions $x=30\text{ m}$ to $x=52\text{ m}$ (around 5 m depth) (Figure 19b). This resistivity anomaly is associated with a cave signal showing resistivity values above 100 Ωm (Figure 19a). Furthermore, at the northern border of the cave, there is an abrupt contact that could be interpreted as a normal fault.

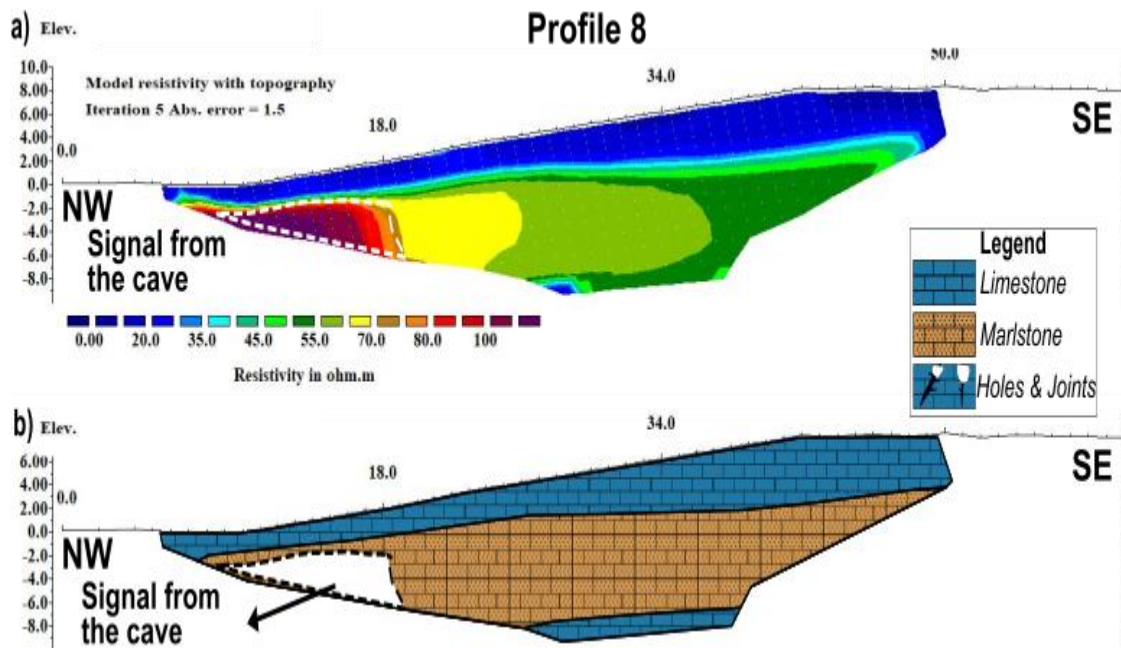


Figure 20. (a) Electrical resistivity section of the ERT profile 8, and (b) sketch of the interpretation of the subsurface geology and cavity model obtained through integration of ERT data and stratigraphy.

The resistivity section of profile 8 (Figure 20a) shows three distinct areas of resistivity. The first unit, $< 40 \Omega\text{m}$, is $\sim 2,5$ m thick at the left-hand corner, and approximately 5 m thick at the right-hand corner. The second layer, ranging from $45 \Omega\text{m}$ to $75 \Omega\text{m}$, is ~ 6 m thick. This unit shows a resistivity anomaly ($> 100 \Omega\text{m}$) that reflects a signal from the cave at the very left-hand side (Labeled in Figure 20b). However, we do not reach the full extent of the cave in this location. In order to do that, we would have needed to start the line $\sim 10\text{-}15$ m more towards left (NW) of the beginning of the survey line. Finally, again a third resistivity unit is displayed showing resistivities below $45 \Omega\text{m}$. The resistivity distribution in profile 8 matches very well with the general electrical distribution inferred from the previous profiles and the stratigraphy.

The inverted section of profile 9 (Figure 21a) reflects two distinctive resistivity units, a more conductive and shallower; and one more resistive and deeper. The shallower unit has resistivity values below $40 \Omega\text{m}$ and its thickness appears thinner at the left-hand corner and thicker at the right-hand corner broadly following the topography. The bottom unit is less conductive with varying upper-boundary depth. Its perceivable thickness (not true thickness, since we do not reach to the bottom of this layer) is ~ 7 m at the left-hand side and ~ 2 m at the right. Furthermore, this layer shows a broad

resistivity anomaly that follows the pitchout of second layer. This anomaly appears at position ~24 – 34 m and is interpreted as signal of the cave (Figure 21b).

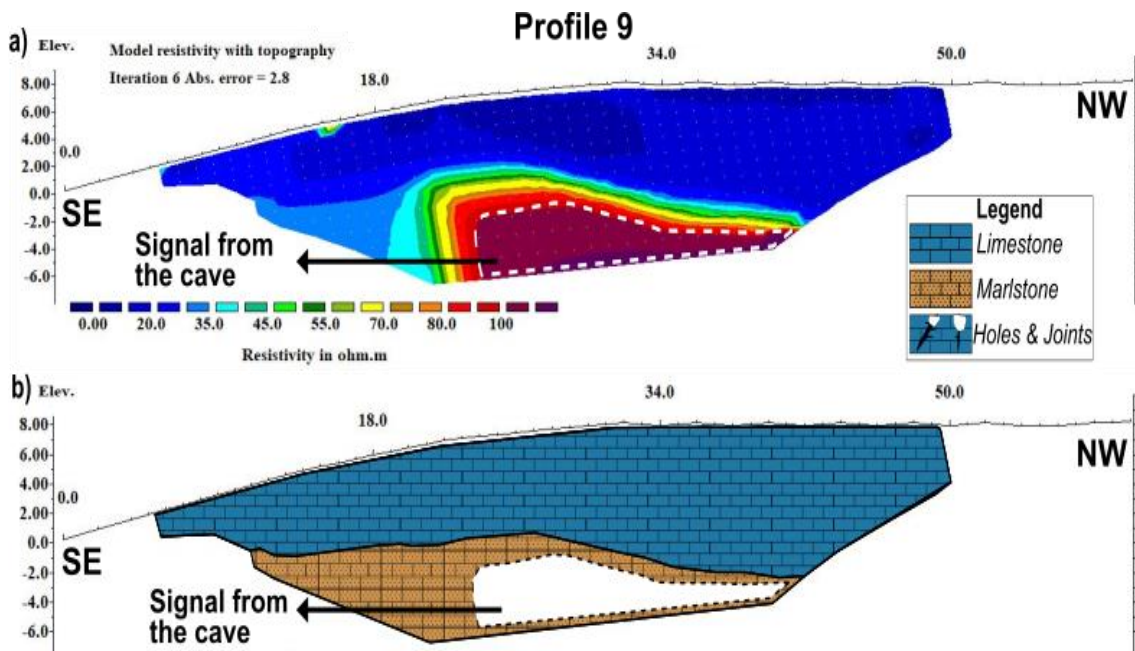


Figure 21. (a) Electrical resistivity section of the ERT profile 9, and (b) sketch of the interpretation of the subsurface geology and cavity model obtained through integration of ERT data and stratigraphy.

On the ERT profile 10 (Figure 22a), the shallowest layer is characterized by electrical resistivity values below 50 Ω m and a thickness that ranges from 2 m to 3 m. In this layer at position $x= 6$ m, there is a superficial hole that creates a resistivity distortion below this position. Underlying the shallowest unit, there is a unit characterized by higher resistivity values (55 Ω m to 75 Ω m), with a thickness of approximately 6 m. Starting from position $x= 18$ m, starts a high electrical resistivity anomaly (>75 Ω m), which indicates evidence of the cave (Figure 22b). Underlying the middle unit, there is a third unit characterized by lower electrical resistivity values below 55 Ω m (similar to unit one), and with a thickness which cannot be defined in absolute terms because we do not reach its bottom.

From profile 11 to profile 13, the surveys were conducted above a part of the cave path where the thickness of the overlying limestone layer is thicker than in previous profiles. These profiles were carried out using the modified dipole-dipole configuration, i.e. modified geometric factor (k), in order to reach deeper depths to detect the cave. Profiles 11, 12 and 13 were repeat profiles with data obtained starting from end of the line towards the start (reciprocal measurements) in order to verify the reliability of the

dipole-dipole method and the modelling (Table 1). Repeated and reciprocal profiles are also done in order to estimate the amount of noise in the data because in the absence of measurement errors or modelling artefacts, repeat and reciprocal profiles should display a similar resistivity distribution.

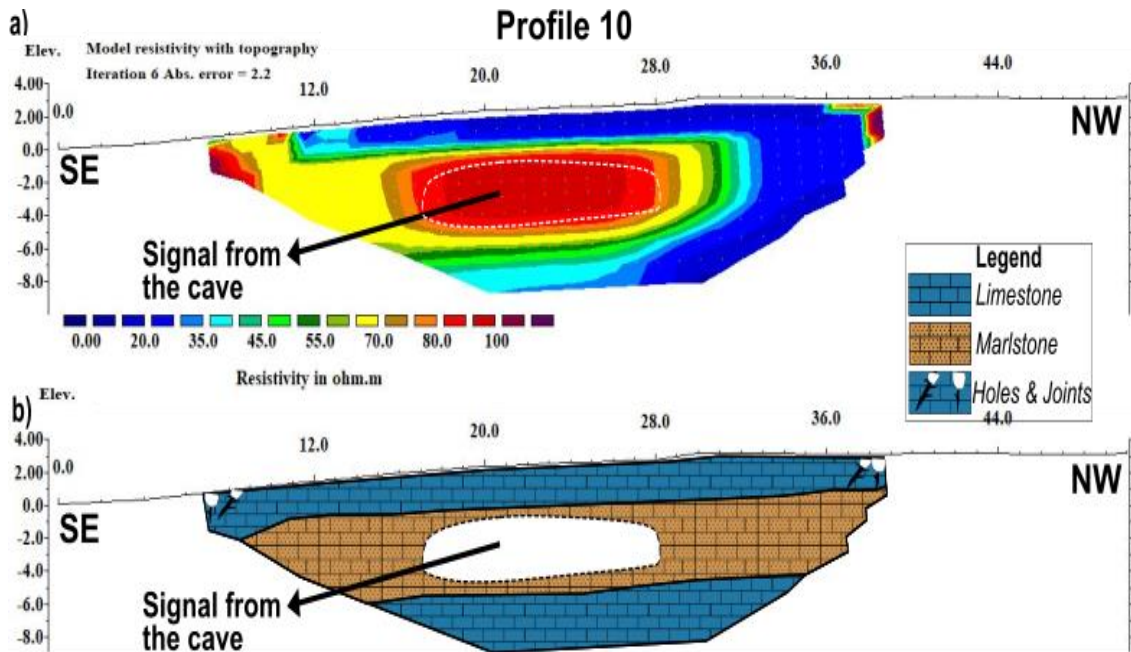


Figure 22. (a) Electrical resistivity section of the ERT profile 10, and (b) sketch of the interpretation of the subsurface geology and cavity model obtained through integration of ERT data and stratigraphy.

The ERT profiles 11 (A to B) and (B to A) (Figures 23a and 23c), show the same resistivity sequence as was described on earlier profiles. These lines run close to the profile 9 and similar to profile 9 they also display two different resistivity units. The upper unit shows values of resistivity below 50 Ω m and it is thinner (~4 m) at “A-side” and thicker (~8 m) at “B-side”. The second unit shows higher resistivity values (55 Ω m to 75 Ω m) with an observable thickness of 8 m. At “A-side”, a high resistivity anomaly (> 85 Ω m) below ~4 m depth is interpreted as a signal from the cave (Figure 23b and 23d). These reciprocal profiles (Figure 23a and 23c) show in general similar change in the resistivity distributions across their profiles with very little differences. The two profiles match with the location of the highest resistivity signals at “A-side” below the topographic low. Furthermore, the two profiles show consistency having similar lowest resistivity zone in the uppermost part of the profile (Labeled as Zone 1, <10 Ω m) (Figure 23a and 23 c).

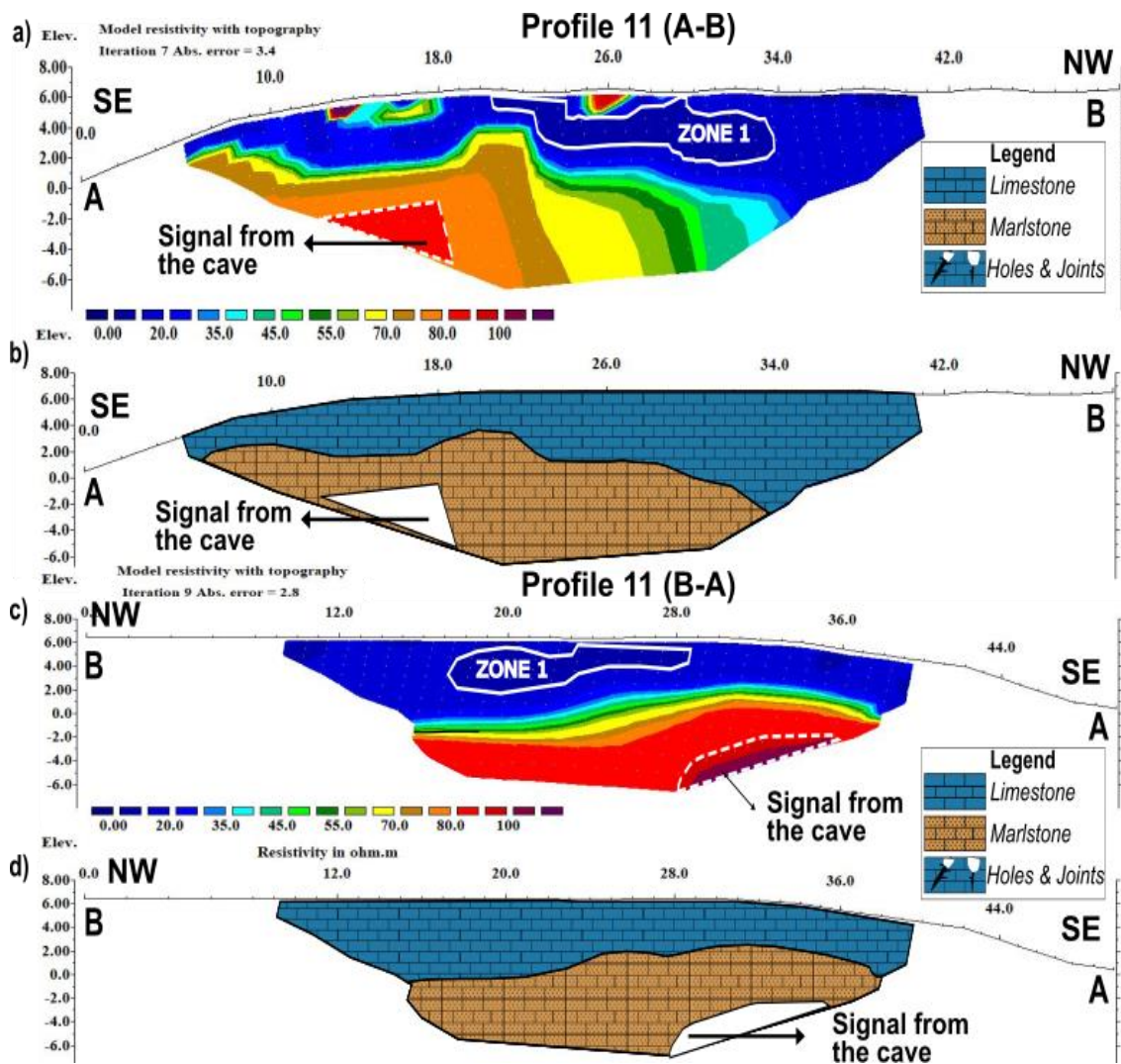


Figure 23. (a) Electrical resistivity section of the ERT profile 11 from A to B and (c) its reciprocal from B to A, and (b and d) sketches of the interpretation of the subsurface geology and cavity model obtained through integration of ERT data and stratigraphy.

The ERT profile 9 (Figure 21a) detects a signal from the cave at depth but it was not able to reach the cave bottom. For this reason, in an attempt to see deeper, the profile 9 was extended 20 meters reaching a total length of 70 m and thereby creating the profile 13 (Table 1). This profile was carried out twice, from A to B and then from B to A both times using the modified geometric dipole-dipole configuration.

Profiles 13 reveals the two resistivity units observed in all previous profiles. The first unit displays resistivities below 35 Ω m (Figure 24a and 24b). In this unit, a more conductive zone ($<10 \Omega$ m, ZONE 1) is clearly defined and it shows the same pattern in the two profiles. In this layer, a resistivity anomaly can be observed at the A-side (labeled as anomaly 2, $> 80 \Omega$ m). This is interpreted as shallow underground holes, whose location was also recorded in the field during the superficial inspection of the survey lines. The

second unit shows resistivities ranging from 45 Ωm to 75 Ωm with an undulatory contact, thicker closer to the A-side. This layer portrays a high-resistivity anomaly ($> 100 \Omega\text{m}$) situated at approximately below 8 m depth measured from the surface. This anomaly is interpreted as being the signal from the cave (Figure 24b and 24d). However, even with the modified dipole configuration we were not able to view the bottom of the cave.

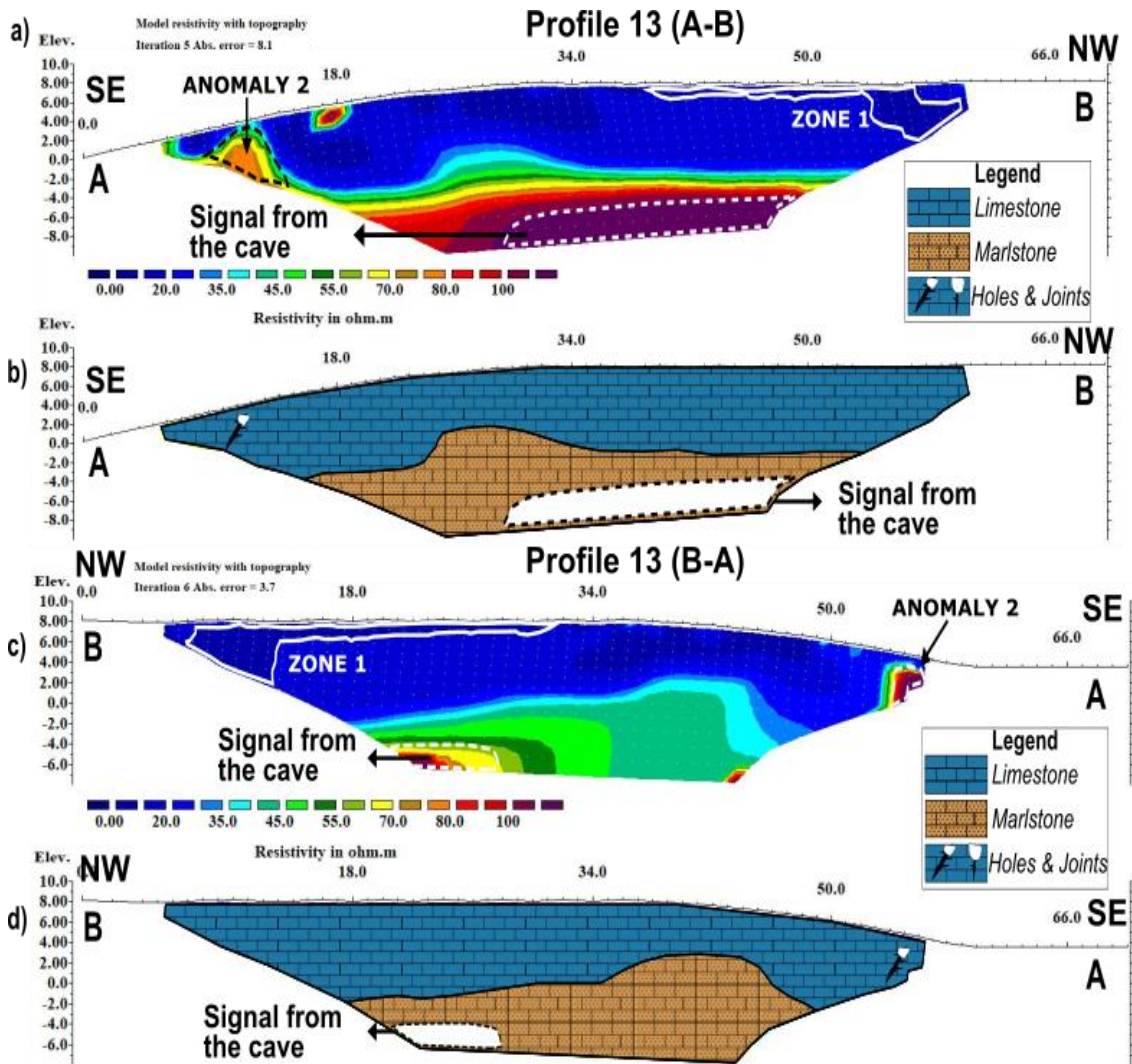


Figure 24. (a) Electrical resistivity section of the ERT profile 13 from A to B and (c) its reciprocal from B to A, and (b and d) sketches of the interpretation of the subsurface geology and cavity model obtained through integration of ERT data and stratigraphy.

Chapter 6 Discussion

Shallow underground caves are contrasting geophysical morphologies and they usually behave as a high resistivity anomaly (Abu-Shariah, 2009). The resistivity contrast between air-filled cavities (high-resistivity) and conductive bedrocks (low-resistivity) creates this anomaly. Based on the geological evidence obtained by the stratigraphy (Figure 14b), speleology and surface exploration, the electrical resistivity region with values below 50 Ωm corresponds to a material composed of bioclastic limestones. Some joints and holes in the bioclastic limestone naturally show significantly high resistivity values, up to 80 to 100 Ωm . Mid-range electrical resistivity values from 51 to 79 Ωm are associated with the marlstone layer (Figure 14b). High resistivity anomalies correlated to cavities are distributed in the marlstone layer showing values from 80 Ωm to >100 Ωm . This interval was taken as starting point to identify an air-filled cavity in the models. Resistivity values of detected cavities vary along the profiles, for instance detected cavities range between 80 and 100 Ωm and in other instances, pronounced cavities reveal resistivities of >100 Ωm . This difference in resistivity can be explained because deeper cavities typically show lower resistivities while shallower cavities higher resistivities. This is due to way the model estimates the resistivities below each point, starting with an assumption of a homogenous half-sphere being under each measurement center point. The performed study indicates that ERT survey is an appropriate technique in cavity detection in the AKS formation. This is verified by the results from the speleology record and from exposed cave passages, where this study was concentrated.

One of the disadvantages of ERT is that each material can be characterized by a wide range of possible resistivities according to the actual physical and chemical conditions of subsoils (Abu-Shariah, 2009; Van Schoor, 2002). However, this disadvantage was not a severe problem for us because underground materials presented well-defined resistivity intervals. These factors are typically seasonally dependent (rain fall, humidity, etc.) and at this location in Ecuador there is little seasonal variation throughout the year. In Tena region of Ecuador, the daytime air temperature does not change during the whole year, but rain intensity and wind vary slightly to produce dry and wet seasons

(Figure 2). The slight variations of the chemical and physical properties of the subsoil in the study area result from the daily heating as well as from the inflow of cold rains.

Another implication of the research is the cave geometry and its relation with the high-resistivity anomalies. The used method and inversion model detected cave passages, but did not have the capacity to provide an exact geometry of them. Anomalies larger than known cave chambers were found in the ERT profiles (see e.g. Profile 2 and 3). Such discrepancy can be explained because high-resistivity zones related to cavities are affected by joints and rock/soil decompaction (Pánek et al., 2010). Another explanation of such singularities is the joints and cracks reaching to the surface at some of the cave passages. This can create magnified resistivity anomalies. Another possibility is the loss of resolution when trying to detect deeper anomalies. A ~3 m cave room below 8 m overburden is likely to give a spread-out signal in the model as we lack data around and beneath it. Determining the cave geometry could be solved in the future by the application of other geophysical methods, such as ground penetrating radar (Beres et al., 2001). However, this method would have very little success in this area due to the high conductive clay type top layer sediments, which would attenuate the electromagnetic waves within the first few tens of centimeters. Other electromagnetic methods such as Slingram style surveying would be a better alternative.

As the first ERT study of this kind in Ecuador, our work tries to define the most suitable technique for cave detection using our homebuilt ERT equipment. Based on similar studies, the choice of the most suitable array is critical in the detection of air-filled cavities. Comparing with the other arrangements, dipole-dipole offers the highest resolution and is most sensitive to lateral variations in resistivity (Putiška et al., 2012). This makes the method especially good for cave detection as long as we do the surveying perpendicular to the cave path. This could explain the problems of lower than usual resistivity values on the only survey line that was taken sub-parallel to the cave (see Annex 2, ERT profile 4). However, there is a caveat, the data collected from dipole-dipole array are easily affected by strong near-surface lateral resistivity variations and therefore can produce noisy data (Zhou et al., 2002). In our case, the typical and modified dipole-dipole configuration (see Annex 1) showed excellent outcomes in the detection of known caves. This finding agrees with comparable studies carried out in

other karst environments (Zhou et al., 2002, 2000). As a remark, the modified dipole-dipole array showed to be dependable and it allowed to reach higher penetration depth without further loss of resolution. There are other possible electrode arrays, and as one recommendation for the future is to test these in the same survey lines for comparison.

Root Mean Square (RMS) error is a typical technique to quantify the error of a model in predicting quantitative data. RMS error measures the data misfit between the measured and calculated apparent resistivity values, i.e. a measure of a goodness of the model suggested by the program to fit the measured data (Loke, 2006). It does not provide us an idea of how truthful the model is. There are cases of acceptable models having an RMS of more than 30 %. The true subsurface can be such that it is hard for the program to estimate and produce. Furthermore, RMS error does not estimate the noise created by occurrence of near-surface resistivity variations, bad ground contact of the electrodes, etc. The real measurement errors are crucial to be detected, if one can, when using geophysical inversion, because they can lead to incorrect resistivity models. With the heightening interest in ERT method, useful tools for assessing the noise levels are needed in order to provide improved inversion images. There are studies (Aster et al., 2018; Binley et al., 1995; Tso et al., 2017) that offer a good review of the use of repeat and reciprocal profiles to evaluate the reliability of the computed inversions. Repeat profiles are carried out anytime at the same electrode locations and remeasured, while reciprocal measurements are made when the start and end locations of profiles are interchanged. In the absence of measurement errors, repeat and reciprocal profiles should display similar images and if they are not identical, noisy data perturbed the ERT inversions.

In order to estimate noise in the data, two repeated profiles (Set 1: Profile 1 and 2; Set 2: Profile 9 and 13) and three reciprocal profiles (Set 3: Profile 11 and 11'; Set 4: Profile 12 and 12'; Set 5: Profile 13 and 13') were carried out in our study.

Set 1 of repeated profiles (Figure 15 and 16) show high similitude between them, but unfortunately, they have different lengths because profile 1 did not detect the cave (Table 1). Despite this inconvenience, the correlated 20 meters between the profiles display almost an identical resistivity distribution even if the profiles were measured months apart. The profiles 1 and 2 show identical conductive layers between them, but

there are some high-resistivity zones that do not match. Specially, at position $x = 20$ m (Figure 14a), profile 1 reflects a high-resistivity anomaly ($<100 \Omega\text{m}$) which is prolonged until the limestone unit, while profile 2 (Figure 15a) shows lower resistivity values ($80 \Omega\text{m}$ to $99 \Omega\text{m}$) that are centered in the marlstone unit. Furthermore, profile 2 displays an unexpected anomaly below the position $x = 12$ m, which is not shown in profile 1. As profile 1 is shorter than profile 2, profile 1 presented variation in the model at the end of them because it has not enough data to display a precise copy of the profile. For this reason, we could not say that these variations are related to noise of the data, but it is clear that the two profiles showed to be consistent to a high degree.

A resistivity correlation of repeated profiles 9 and 13 (A to B) is presented in Figure 25. In order to appreciate better the similitudes between these profiles, ERT profile 13 was shortened 20 meters and adapted to the scale of profile 9. At the left-side of profiles, there is no exact similitude between them, but the inversions seem to be consistent in contrasting resistivity zones. Profile 13 compared to profile 9 (Figure 25) appears to be more sensitive to a near-surface resistivity anomaly which created a distortion in the resistivity distribution. From position $x = 18$ m, the repeated profiles look more similar showing correlative resistivity zones. The upper layer (limestone) shows very conductive zones (white dashed lines, Figure 25) that are consistent in the two profiles. Although the geometry of these conductive zones is not exactly similar, these zones display resemblances with respect to their shape and behavior. At the bottom of both profiles, a zone labeled as A is shown in order to illustrate the high similarities between the ERT profiles, interpreted as the cave signal. From the right to position $x = 24$ m, the A zones match in geometry, size and thickness, but from $x = 24$ m to the left the profiles differ. This difference is likely due to noise in the data originated by the choice of the electrode array – the high sensitivity of dipole-dipole array to near-surface resistivity variations. Profile 13 detects the resistivity variation below position $x = 12$ m more strongly than profile 9, but as this variation is in the surface, it can obscure the resistivity values in the surrounding area creating a false resistivity distribution deeper down. This distribution is likely wrong because it has no sense with the stratigraphy. This example highlights the importance of knowing the local geology and stratigraphy of the study area before interpreting the geophysical data. Every geophysical survey has to be combined with a

geological and stratigraphical analysis from either existing literature, borehole exploration data, and/or outcrops and other exposures.

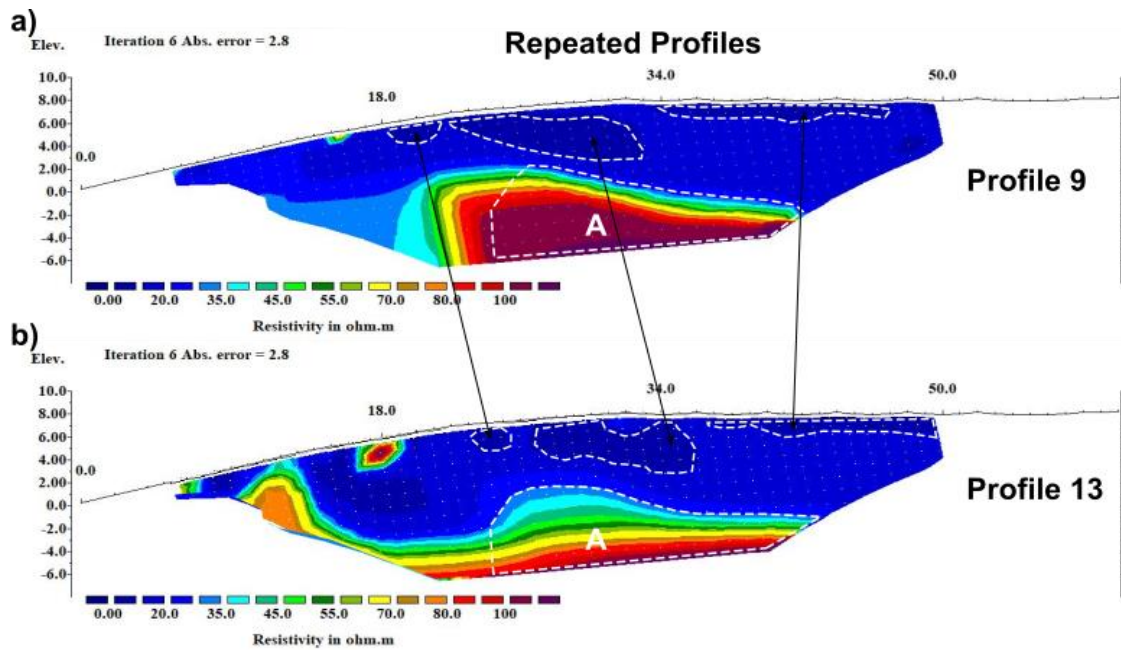


Figure 25. Repeated profile showing resistivity correlation (White dashed lines) (a) Electrical resistivity section of the ERT profile 9 and (b) Electrical resistivity section of the ERT profile 13 (A to B).

Chapter 7 Conclusions

- The main purpose of this research was to assess the ERT technique for detecting shallow caves located in AKS. The ERT technique appropriately differentiated three stratigraphic layers in the UICC. The results shows three geologic layers: (1) a top layer of ~2 to 9-m-thick (< 50 Ωm - limestones); (2) a middle layer of ~2 to 4-m-thick (51–80 Ωm - marlstone); (3) another limestones intercalation (< 50 Ωm); and an cave signal (80 to >100 Ωm). The profiles portrayed a high-resistivity anomaly that was first verified to correspond to the signal from the cave in known locations above the surface, along the cave path, with a cave ceiling placed between ~3 m to ~8 m below the surface. The method was then further successfully tested in other areas along the cave path where its exact location was not known. The ERT method proved to be very useful in detecting the location of the shallow cavities at the UICC area. Furthermore, this geophysical technique showed the occurrence of possible unknown caves/cavities in the area and possible faulting blocks.
- The choice of the most suitable electrode arrangement for resistivity prospecting requires knowledge of a) the geological properties of the study area, and b) the sensitivity of each array to a certain geomorphology. This study demonstrated that the modified dipole-dipole array was the best fit for our given task, because it significantly increased the theoretical depth of the profiles without a significant increase in noise.
- The 2D ERT inversions were employed to also determine the geometry of known shallow cavities, but the results showed that the technique does not have the capacity to determine a precise geometry of them.
- The precision in detecting the cave was generally excellent, with only some minor limitations where the caves are situated deeper underneath a thick overburden. The situation is especially difficult if the cave is deep and there are additional shallow cavities or other drastic changes in the resistivities in the top-most layer. This is due to the drawback of the dipole-dipole array, which is easily affected by near-surface resistivity variations. Nevertheless, the approximate location of these deeper cave locations was still identified.

Chapter 8 Future Work and Recommendations

- In order to have a better estimation of the noise errors, repeated and reciprocal profiles should always be carried out for each profile, and their 2D inversions should be compared. This would increase the data collection time but allows to better evaluate the amount of noise error for each profile and increase the signal to noise ratio.
- The ERT technique using a dipole-dipole array should only be employed perpendicular to the cave path. It is because this array is well suited for detecting horizontal objects (such as dikes, caves, and fractures), but it is not particularly sensitive to vertical changes in resistivity (sedimentary layers).
- Future work at the UICC cave should include continuing the survey lines along the whole cave path. Furthermore, it should be done using the modified dipole-dipole array and following the above recommendations.
- In order to have a better correlation of the stratigraphic section with respect to the local geological setting, dating of the calcareous limestone should be carried out in order to determine the age the UICC limestones.
- Considering the Tamia Yura community lack some essential information of the UICC, it would be recommended to elaborate and hand out to the city GAD a detailed map describing the cave path projected on a topographic map with some cross-sections showing the internal shape of the cave underneath. This document would be really useful for the guided visits to the tourists as well as a helpful memo for the community on which locations they should not plan constructing building or roads etc. thereby preventing cave collapses.

Annexes

Annex 1

1) Derivation of the geometric factor for a typical dipole-dipole configuration.

Modified Dipole - Dipole Geometric Factor

Piispa, Elisa Johanna; Chamba Vásquez, Bryan Antonio
School of Earth Science, Energy and Environment, Yachay Tech

May 27, 2020

1 Geometric Factor for a typical Dipole-Dipole Configuration

The derivations are based on the assumption that arrangements consist of a pair of current electrodes (A, B) and a pair of potential electrodes (C, D). In general, the value of the geometric factor K for any quadrupole array can be computed from the expression (Heiland, 1940).

$$K = \left[\frac{1}{r_1} - \frac{1}{r_2} - \frac{1}{r_3} + \frac{1}{r_4} \right]^{-1} \quad (1)$$

Where $r_1, r_2, r_3,$ and r_4 are the distances $R_{AC}, R_{AD}, R_{BC},$ and R_{BD} between the current electrodes, A and B , and the potential electrodes, C and D (Fig. 1). In the double-dipole configuration (Fig. 1), the spacing of the electrodes in each pair is a , while the distance between their mid-points is L . Note that (fig. 1) shows an electrode array where the current electrodes A and B were flipped to have the electrode D defined as the potential electrode closer to current sink A . In order to calculate the geometric factor for a dipole-dipole electrode configuration, we use the electrode sorting showed in Figure 1.

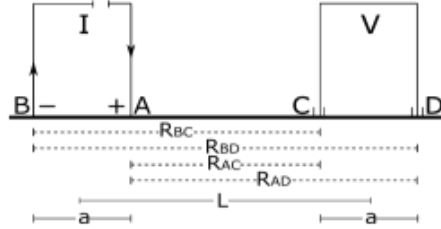


Figure 1: Typical Dipole-Dipole arrangement

Using the electrode spacing "a" and "L", we could defined the following expressions:

$$R_{AC}=L-a; R_{BC}=L; R_{AD}=L; R_{BD}=L+a$$

Substituting these expression in equation 1, we get:

$$\begin{aligned} \frac{1}{K} &= \left[\frac{1}{L-a} - \frac{1}{L} - \frac{1}{L} + \frac{1}{L+a} \right] \\ \frac{1}{K} &= \left[\frac{L-L+a}{(L-a)L} - \frac{L+a-L}{(L-a)L} \right] \\ \frac{1}{K} &= \left[\frac{a}{(L-a)L} - \frac{a}{(L-a)L} \right] \\ \frac{1}{K} &= \left[\frac{(L+a)a - (L-a)a}{L(L^2-a^2)} \right] \\ \frac{1}{K} &= \left[\frac{La+a^2-La+a^2}{L(L^2-a^2)} \right] \\ \frac{1}{K} &= \left[\frac{2a^2}{L(L^2-a^2)} \right] \\ K &= \left[\frac{L(L^2-a^2)}{2a^2} \right] \end{aligned} \quad (2)$$

2) Derivation of the geometric factor for a modified dipole-dipole configuration

2 Geometric Factor for a modified Dipole-Dipole Configuration

In the typical Dipole-Dipole arrangement, the electrode spacing "a" is equal and maintained constant all times. A modified Dipole-Dipole arrangement the spacings between the current electrodes AB, and the potential Electrodes CD are different. It means that the spacing between current electrodes is "a₁" while the spacing between potential electrodes is "a₂" (Fig. 2).

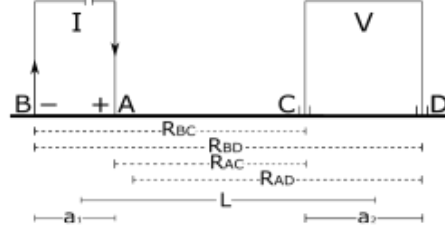


Figure 2: Modified Dipole-Dipole arrangement

Using the electrode spacing "a₁", "a₂" and "L", we could defined the following expressions:

$$R_{AC} = L - \frac{a_1}{2} - \frac{a_2}{2} = \frac{2L - a_1 - a_2}{2}; \quad R_{BC} = L + \frac{a_1}{2} - \frac{a_2}{2} = \frac{2L + a_1 - a_2}{2};$$

$$R_{AD} = L - \frac{a_1}{2} + \frac{a_2}{2} = \frac{2L - a_1 + a_2}{2}; \quad R_{BD} = L + \frac{a_1}{2} + \frac{a_2}{2} = \frac{2L + a_1 + a_2}{2}.$$

Substituting these expression in equation 1, we get:

$$\begin{aligned} \frac{1}{K} &= 2 \left[\frac{1}{2L - a_1 - a_2} - \frac{1}{2L + a_1 - a_2} - \frac{1}{2L - a_1 + a_2} + \frac{1}{2L + a_1 + a_2} \right] \\ \frac{1}{K} &= 2 \left[\frac{2L + a_1 - a_2 - 2L + a_1 + a_2}{(2L - a_2)^2 - a_1^2} + \frac{-2L - a_1 - a_2 + 2L - a_1 + a_2}{(2L - a_2)^2 - a_1^2} \right] \\ \frac{1}{K} &= 2 \left[\frac{2a_1}{(2L - a_2)^2 - a_1^2} - \frac{2a_1}{(2L - a_2)^2 - a_1^2} \right] \\ \frac{1}{K} &= 2 \left[\frac{2a_1 [(2L + a_2)^2 - a_1^2] - 2a_1 [(2L - a_2)^2 - a_1^2]}{(2L - a_2)^2 - a_1^2} \right] \\ \frac{1}{K} &= 2 \left[\frac{2a_1 (4L^2 + 4La_2 + a_2^2) - 2a_1 (4L^2 - 4La_2 + a_2^2)}{(2L - a_2)^2 - a_1^2} \right] \\ \frac{1}{K} &= 2 \left[\frac{8L^2 a_1 + 8La_1 a_2 + 2a_1 a_2^2 - 8L^2 a_1 + 8La_1 a_2 - 2a_1 a_2^2}{(2L - a_2)^2 - a_1^2} \right] \\ \frac{1}{K} &= \left[\frac{32La_1 a_2}{(2L - a_2)^2 - a_1^2} \right] \\ K &= \left[\frac{(2L - a_2)^2 - a_1^2}{32La_1 a_2} \right] \end{aligned} \quad (3)$$

References

Heiland, C. (1940). Geophysical exploration: Hanfner publ. Co., 1013, New York.

Annex 2

1) ERT profile 4

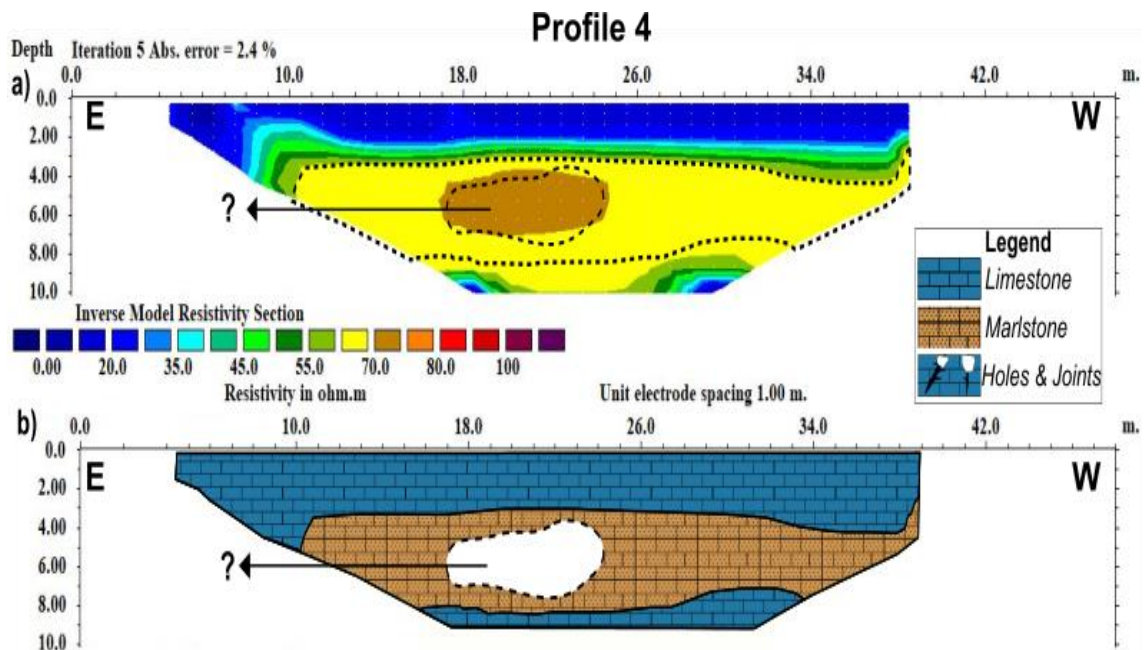


Figure A1. (a) Electrical resistivity section of the ERT profile 4, and (b) sketch of the interpretation of the subsurface geology and cavity model obtained through integration of ERT data and stratigraphy.

ERT profile 4 was intended to be taken subparallel to the cave room at the window (Figure A1). It shows three distinctive resistivity units but they have lower resistivity values in general than the other profiles. In Figure A1a, a more conductive unit can be seen ($< 50 \Omega\text{m}$), associated with the overburden on top of the cave with an average thickness of ~ 3.5 m. Underlying this first unit, there is a flat unit showing the highest resistivity values ($50 \Omega\text{m}$ to $65 \Omega\text{m}$). The geometry of this layer coincides with the shape of the cave room close to the window (2.5 m to 4 m height), but the values of resistivity are lower than the values interpreted as an air-filled void. Finally, profile 4 shows a gently undulating resistivity geometry ($< 50 \Omega\text{m}$) at the bottom of cave located at a depth of approximately > 8 m, which coincides fairly well with the cave floor (Figure A1b). There is no high resistivity signal from the cave registered in this profile. However, based on the speleology and field observation on top of the surface (e.g. location of the window with respect to this survey line), we know that this profile crosses through the window cave room approximately at position $x = 15$ m. Coincidentally, in this position is located a peak resistivity ($70 \Omega\text{m}$), but again this value is lower than the expected. The

probable reason for the absence of a high resistivity anomaly in this profile is explained in the discussion.

2) ERT profile 5

In Figure A2a is shown profile 5, which runs close to the profile 3 but with a different orientation and in a zone with a different topography. Unfortunately, at this location, the dense vegetation did not allow recording reliable GPS data for variations in the topography. The upper unit of this profile reaches deeper (~6 m) than in previous profiles with resistivity values below 55 Ωm . A second unit is observed showing high resistivity values over 100 Ωm . The contact between unit one and two appears to be variable being shallower during the first 10 – 15 m followed by thicker part from ~15 m to ~30 m. This could reflect variable level of erosion or it can be an artefact of the modelling, since it is observed at the very edges of the 2D model, which are more prone to erroneous interpretations. Starting from ca. meter 30 to the end of the profile a high resistivity anomaly reaching throughout the whole section can be seen. This signal is interpreted to correspond crossing the path of the cave (Figure A2b).

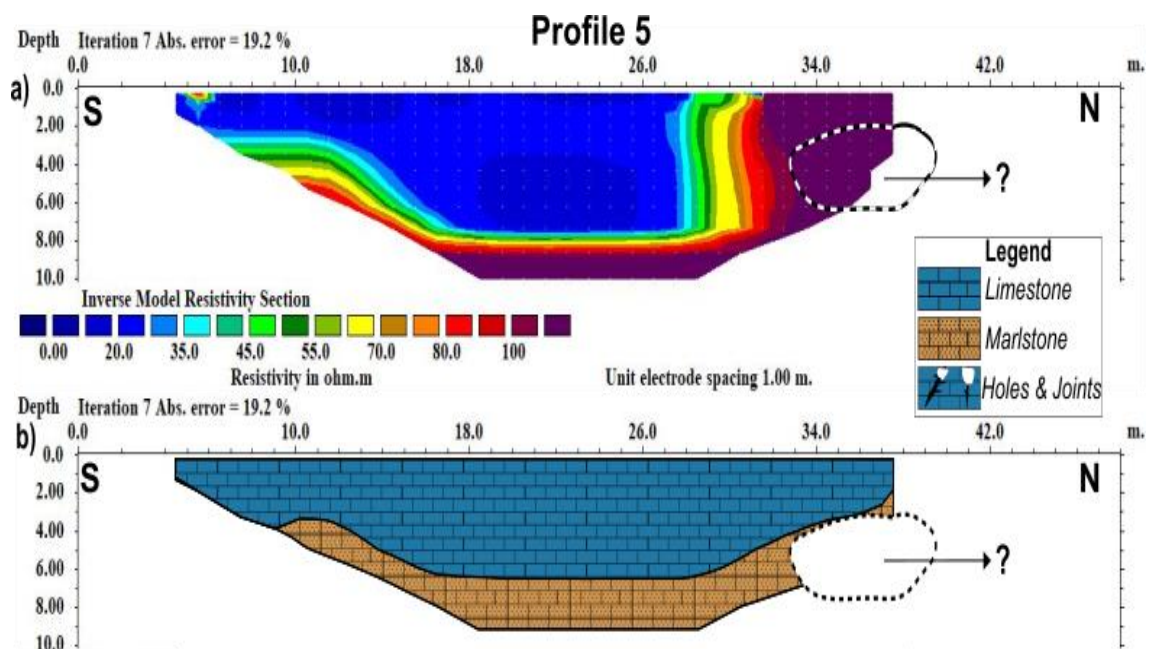


Figure A2. (a) Electrical resistivity section of the ERT profile 5, and (b) sketch of the interpretation of the subsurface geology and cavity model obtained through integration of ERT data and stratigraphy.

3) ERT profiles 12

The ERT profiles 12 (A to B) and (B to A) (Figures A3a and A3c), are characterized by sharp contrast between the two resistivity zones. The first unit shows low values of resistivity ($<50 \Omega\text{m}$) and its thickness ($\sim 5 \text{ m}$) is thinner at the “A-side” and thicker ($\sim 9 \text{ m}$) at “B-side”. A second unit displays higher resistivity values ($55 \Omega\text{m}$ to $75 \Omega\text{m}$) and its observable (not real) thickness ranges from 2 m to 4 m moving from left to right. At “A” side, a high resistivity anomaly ($> 100 \Omega\text{m}$) at depth of 6 m is labeled as the signal from the cave (Figure A3b and A3d). Again, the two profiles show similar patterns in their resistivity distribution displaying a similar more conductive area (labeled as ZONE 1, Figure A3a and A3c) at the shallower part of their profiles.

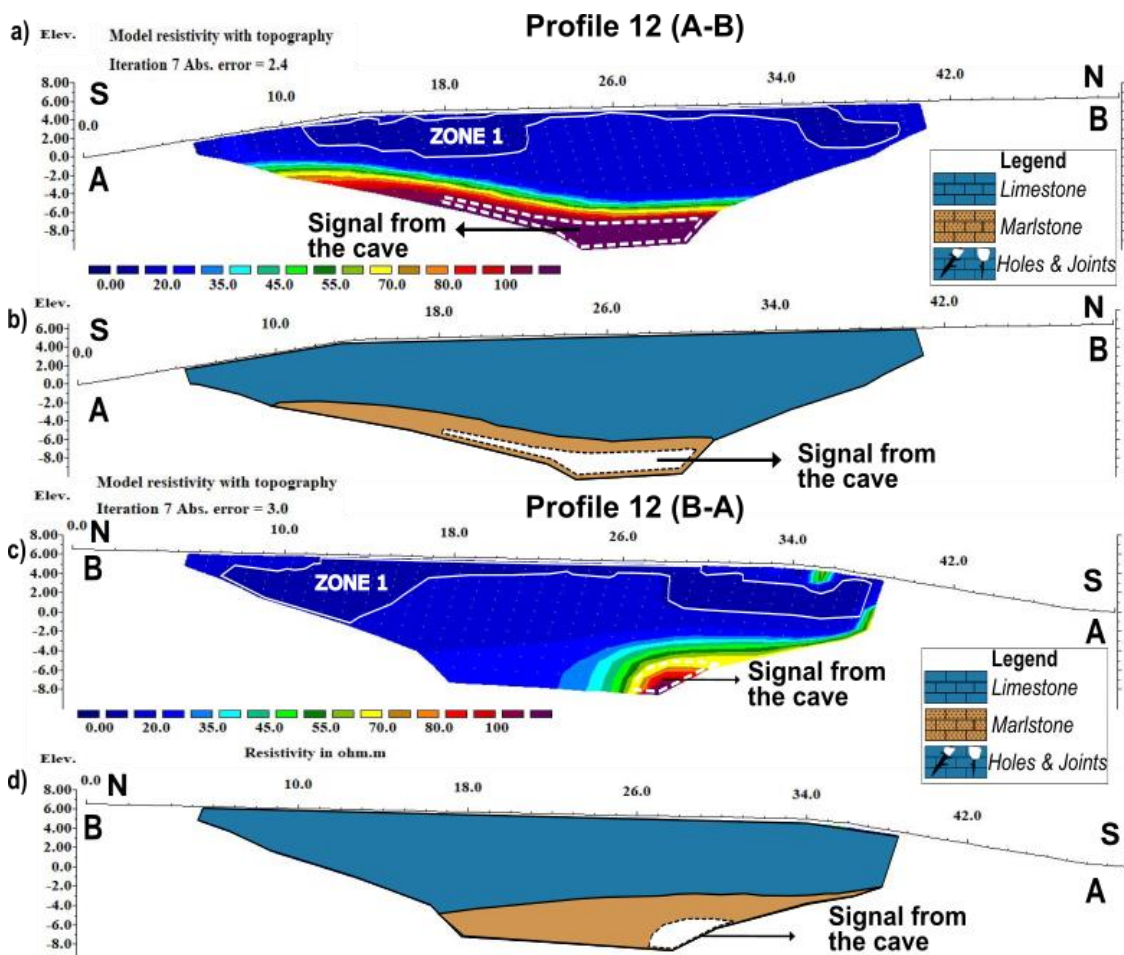


Figure A3. (a) Electrical resistivity section of the ERT profile 12 from A to B and (c) its reciprocal from B to A, and (b) and (d) sketch of the interpretation of the subsurface geology and cavity model obtained through integration of ERT data and stratigraphy.

References

- Abu-Shariah, M. I. I. (2009). Determination of cave geometry by using a geoelectrical resistivity inverse model. *Engineering Geology*, 105(3–4), 239–244.
- Almeida, J. P. (1986). Estudio de litofacies y del Contacto Agua-Petroleo de la Arenisca ‘T’ del Campo Libertador. *Memoria Tomo III: Geología Del Petróleos Ingeniería de Petróleos, I*, 119–148.
- Arteaga Pozo, M. E. (2019). *Subsurface water flow assessed with electrical resistivity and ground-penetrating radar in yachay tech, Ecuador*. Universidad de Investigación de Tecnología Experimental Yachay.
- Aster, R. C., Borchers, B., & Thurber, C. H. (2018). *Parameter estimation and inverse problems*. Elsevier.
- Bastidas, A. (2019). *Caracterización de impactos ambientales por actividades turísticas en cavernas Jumandy, provincia de Napo*. Facultad de Ciencias Naturales. Universidad de Guayaquil.
- Benson, A. K. (1995). Applications of ground penetrating radar in assessing some geological hazards: examples of groundwater contamination, faults, cavities. *Journal of Applied Geophysics*, 33(1–3), 177–193.
- Beres, M., Luetscher, M., & Olivier, R. (2001). Integration of ground-penetrating radar and microgravimetric methods to map shallow caves. *Journal of Applied Geophysics*, 46(4), 249–262.
- Binley, A., Ramirez, A., & Daily, W. (1995). Regularised image reconstruction of noisy electrical resistance tomography data. *Proceedings of the 4th Workshop of the European Concerted Action on Process Tomography, Bergen, Norway*, 401–410.
- Bozigar, M., Gray, C. L., & Bilsborrow, R. E. (2016). Oil extraction and indigenous livelihoods in the northern Ecuadorian Amazon. *World Development*, 78, 125–135.
- Burke, K. C., & Lytwyn, J. (1993). Origin of the rift under the Amazon basin as a result of continental collision during Pan-African time. *International Geology Review*, 35(10), 881–897.
- Cardarelli, E., Di Filippo, G., & Tuccinardi, E. (2006). Electrical resistivity tomography to detect buried cavities in Rome: a case study. *Near Surface Geophysics*, 4(6), 387–392.
- Chilingar, G. V. (1956). Soviet Classification of Sedimentary Particles and Vasil’evskiy Graph. *AAPG Bulletin*, 40(7), 1714–1715.
- Clark, J. A., & Page, R. (2011). Inexpensive Geophysical Instruments Supporting Groundwater Exploration in Developing Nations. *Journal of Water Resource and Protection*, 03(10), 768–780. <https://doi.org/10.4236/jwarp.2011.310087>
- CLIMATE-DATA.ORG. (2019). Datos climáticos de Tena. website: <https://es.climate-data.org/americas-del-sur/ecuador/provincia-de-napo/tena-2977/>
- Constantin, S., Toulkeridis, T., Moldovan, O. T., Villacís, M., & Addison, A. (2019). Caves and karst of Ecuador—state-of-the-art and research perspectives. *Physical Geography*, 40(1), 28–51. <https://doi.org/10.1080/02723646.2018.1461496>
- Dashwood, M. F., & Abbotts, I. L. (1990). Aspects of the petroleum geology of the Oriente Basin, Ecuador. *Geological Society Special Publication*, 50(50), 89–117. <https://doi.org/10.1144/GSL.SP.1990.050.01.06>
- Davies, W. E., & Morgan, I. M. (1987). *Geology of caves: US Geological Survey*.
- Debut, A., Guerra, S., & Toulkeridis, T. (2015). Bacterias recolectadas en las cuevas Castillo y Gruta de Virgen en la Provincia de Napo. *3er Simposio Internacional de Espeleología En El Ecuador-Boletín Científico*, 104.

- Foss, J. E., Moormann, F. R., & Rieger, S. (1983). Inceptisols. In *Developments in Soil Science* (Vol. 11, pp. 355–381). Elsevier.
- Frisia, S., & Borsato, A. (2010). Chapter 6 Karst. *Developments in Sedimentology*, 61(C), 269–318. [https://doi.org/10.1016/S0070-4571\(09\)06106-8](https://doi.org/10.1016/S0070-4571(09)06106-8)
- Gambetta, M., Armadillo, E., Carmisciano, C., Stefanelli, P., Cocchi, L., & Tontini, F. C. (2011). Determining geophysical properties of a near-surface cave through integrated microgravity vertical gradient and electrical resistivity tomography measurements. *Journal of Cave and Karst Studies*, 73(1), 11–15. <https://doi.org/10.4311/jcks2009ex0091>
- Gonzales, A., Maldonado, F., & Mejía, L. (1986). Memoria Explicativa del mapa general de suelos del Ecuador, Sociedad Ecuatoriana de la ciencia del suelo. *Quito, Ecuador*, 23.
- Heiland, C. A. (1940). Exploration geophysics. *NY: Prentice–Hall*.
- Herman, R. (2001). An introduction to electrical resistivity in geophysics. *American Journal of Physics*, 69(9), 943–952.
- Jaillard, E., Bengtson, P., & Dhondt, A. V. (2005). Late Cretaceous marine transgressions in Ecuador and northern Peru: A refined stratigraphic framework. *Journal of South American Earth Sciences*, 19(3), 307–323. <https://doi.org/10.1016/j.jsames.2005.01.006>
- Jones, C. (2009). *A guide to responsible caving*. National Speleological Society.
- Kléver, R. (2014). *Actualización plan de desarrollo y ordenamiento territorial*. Tena.
- Loke, D. M. (2000). Electrical imaging surveys for environmental and engineering studies - A practical guide to 2-D and 3-D surveys Copyright. *Cangkat Minden Lorong, August 200(1999)*, 61.
- Loke, M. H. (2006). RES2DINV ver. 3.55 for Windows 98/Me/2000/NT/XP, Rapid 2-D Resistivity & IP inversion using the least-squares method. *GEOTOMO SOFTWARE, Software Manual*.
- Loke, M. H., Acworth, I., & Dahlin, T. (2003). A comparison of smooth and blocky inversion methods in 2D electrical imaging surveys. *Exploration Geophysics*, 34(3), 182–187. <https://doi.org/10.1071/EG03182>
- Lowrie, W. (2007). Fundamentals of Geophysics. In *Fundamentals of Geophysics*. <https://doi.org/10.1017/cbo9780511807107>
- Lowrie, W., & Fichtner, A. (2019). *Fundamentals of geophysics*. Cambridge university press.
- Manatsa, D., Chingombe, W., & Matarira, C. H. (2008). The impact of the positive Indian Ocean dipole on Zimbabwe droughts Tropical climate is understood to be dominated by. *International Journal of Climatology*, 2029(March 2008), 2011–2029. <https://doi.org/10.1002/joc>
- Martínez-Pagán, P., Gómez-Ortiz, D., Martín-Crespo, T., Manteca, J. I., & Rosique, M. (2013). The electrical resistivity tomography method in the detection of shallow mining cavities. A case study on the Victoria Cave, Cartagena (SE Spain). *Engineering Geology*, 156, 1–10. <https://doi.org/10.1016/j.enggeo.2013.01.013>
- McDonald, R., & Davies, R. (2003). Integrated geophysical surveys applied to karstic studies. *First Break*, 21(10).
- Metwaly, M., & Alfouzan, F. (2013). Application of 2-D geoelectrical resistivity tomography for subsurface cavity detection in the eastern part of Saudi Arabia. *Geoscience Frontiers*, 4(4), 469–476. <https://doi.org/10.1016/j.gsf.2012.12.005>
- Nouvelot, J.-F., Le Goulven, P., Aleman, M., & Pourrut, P. (1995). Análisis estadístico y regionalización de las precipitaciones en el Ecuador. *El Agua En El Ecuador : Clima, Precipitaciones, Escorrentia*, 27–66. Retrieved from

- <http://www.documentation.ird.fr/hor/fdi:010014828>
- Ortega, A. I., Benito-Calvo, A., Porres, J., Pérez-González, A., & Martín Merino, M. A. (2010). Applying electrical resistivity tomography to the identification of endokarstic geometries in the Pleistocene Sites of the Sierra de Atapuerca (Burgos, Spain). *Archaeological Prospection*, 17(4), 233–245.
<https://doi.org/10.1002/arp.392>
- Padilla, O., Kirby, E., Sani, J. C., & Duque, M. J. (2015). Uso y procesamiento del sistema escáner láser para el levantamiento 3D para aplicaciones espeleológicas. *3er Simposio Internacional de Espeleología En El Ecuador-Boletín Científico*, 68.
- Pánek, T., Margielewski, W., Tábořík, P., Urban, J., Hradecký, J., & Szura, C. (2010). Gravitationally induced caves and other discontinuities detected by 2D electrical resistivity tomography: Case studies from the Polish Flysch Carpathians. *Geomorphology*, 123(1–2), 165–180.
<https://doi.org/10.1016/j.geomorph.2010.07.008>
- Pemberthy, M. (2019). *Evaluación de la concentración de radón en cuevas turísticas de la provincia de Napo*. Quito: Universidad de las Américas, 2019.
- Putiška, R., Nikolaj, M., Dostál, I., & Kušnirák, D. (2012). Determination of cavities using electrical resistivity tomography. *Contributions to Geophysics and Geodesy*, 42(2), 201–211.
- Sánchez Cortez, J. L. (2017). *Guía Espeleológica de Napo*. 106.
- Sasaki, Y. (1986). Two-dimensional joint inversion of magnetotelluric and dipole data. *1986 SEG Annual Meeting, SEG 1986*, 54(2), 55–57.
<https://doi.org/10.1190/1.1892904>
- Sciotti, M. (1982). Engineering geological problems due to old underground quarries in the urban area of Rome (Italy). *International Association of Engineering Geology. International Congress*. 4, 211–225.
- Terry, R. D., Chilingar, G. V., & Hancock, A. (1955). Comparison charts for visual estimation of percentage composition. *Journal of Sediment Petrology*, 25, 229–234.
- Todd, D. K., & Mays, L. W. (2005). Groundwater hydrology edition. *Welly Inte*.
- Toulkeridis, T., Addison, A., Constantin, S., Winkler, E., Toomey III, R., Osburn, R., ... Addison, A. (2015). Espeleología en Tena, Napo. Un breve inventario geológico y cartográfico. *3er Simposio Internacional de Espeleología En El Ecuador-Tena. Boletín Científico. Imprenta de La Universidad de Las Fuerzas Armadas-ESPE, Sangolquí*, 26–67.
- Toulkeridis, T., Fuertes, W., Carrera, D., Delgado, V., Villacís, C., Galárraga, F., & Aules, H. (2015). Medición de diferentes gases potencialmente responsables del efecto invernadero, calentamiento global y cambio climático en tiempo real en Cuevas de las Provincias Napo, Pastaza y Galápagos. *3er Simposio Internacional de Espeleología En El Ecuador-Boletín Científico*, 110.
- Tso, C.-H. M., Kuras, O., Wilkinson, P. B., Uhlemann, S., Chambers, J. E., Meldrum, P. I., ... Binley, A. (2017). Improved characterisation and modelling of measurement errors in electrical resistivity tomography (ERT) surveys. *Journal of Applied Geophysics*, 146, 103–119.
- Van Schoor, M. (2002). Detection of sinkholes using 2D electrical resistivity imaging. *Journal of Applied Geophysics*, 50(4), 393–399.
- White, H. J., Skopec, R. A., Ramirez, F. A., Rodas, J. A., & Bonilla, G. (1995). *Reservoir characterization of the Hollin and Napo formations, western Oriente Basin, Ecuador*.
- Zhou, W., Beck, B. F., & Adams, A. L. (2002). Effective electrode array in mapping

karst hazards in electrical resistivity tomography. *Environmental Geology*, 42(8), 922–928.

Zhou, W., Beck, B. F., & Stephenson, J. B. (2000). Reliability of dipole-dipole electrical resistivity tomography for defining depth to bedrock in covered karst terranes. *Environmental Geology*, 39(7), 760–766.